Article

Fatty acid chain length drives lysophosphatidylserine-dependent immunological outputs

Neha Khandelwal,[1,5] Minhaj Shaikh,[2,5] Amol Mhetre,[1,5,*] Shubham Singh,[1,5] Theja Sajeevan,[1] Alaumy Joshi,[1,4] Kithiganahalli Narayanaswamy Balaji,[3] Harinath Chakrapani,[2,*] and Siddhesh S. Kamat[1,6,*]

[1]Department of Biology, Indian Institute of Science Education and Research (IISER) Pune, Dr. Homi Bhabha Road, Pashan, Pune, Maharashtra 411008, India
[2]Department of Chemistry, Indian Institute of Science Education and Research (IISER) Pune, Dr. Homi Bhabha Road, Pashan, Pune, Maharashtra 411008, India
[3]Department of Microbiology and Cell Biology, Indian Institute of Science (IISc), Bangalore, Karnataka 560012, India
[4]Present address: Department of Biochemistry & Biophysics, Texas A&M University, College Station, TX 77843, USA
[5]These authors contributed equally
[6]Lead contact
*Correspondence: amol@iiserpune.ac.in (A.M.), harinath@iiserpune.ac.in (H.C.), siddhesh@iiserpune.ac.in (S.S.K.)
https://doi.org/10.1016/j.chembiol.2021.01.008

SUMMARY

In humans, lysophosphatidylserines (lyso-PSs) are potent lipid regulators of important immunological processes. Given their structural diversity and commercial paucity, here we report the synthesis of methyl esters of lyso-PS (Me-lyso-PSs) containing medium- to very-long-chain (VLC) lipid tails. We show that Me-lyso-PSs are excellent substrates for the lyso-PS lipase ABHD12, and that these synthetic lipids are acted upon by cellular carboxylesterases to produce lyso-PSs. Next, in macrophages we demonstrate that VLC lyso-PSs orchestrate pro-inflammatory responses and in turn neuroinflammation via a Toll-like receptor 2 (TLR2)-dependent pathway. We also show that long-chain (LC) lyso-PSs robustly induce intracellular cyclic AMP production, cytosolic calcium influx, and phosphorylation of the nodal extracellular signal-regulated kinase to regulate macrophage activation via a TLR2-independent pathway. Finally, we report that LC lyso-PSs potently elicit histamine release during the mast cell degranulation process, and that ABHD12 is the major lyso-PS lipase in these immune cells.

INTRODUCTION

Lipids have long been known as potent signaling molecules that mediate many important physiological processes in mammals, including humans (Wymann and Schneiter, 2008; Dennis, 2016; Fahy et al., 2005). Prominent among the signaling lipids are the prostaglandins (Dennis and Norris, 2015), the endocannabinoids (2-arachidonoylglycerol [2-AG] and anandamide [AEA]) (Blankman and Cravatt, 2013; Fowler et al., 2005), and the well-studied lysophospholipids, sphingosine 1-phosphate (S1P) (Gonzalez-Cabrera et al., 2014; Rosen et al., 2013) and lysophosphatidic acid (lyso-PA) (Ishii et al., 2004; Contos et al., 2000). Given their physiological importance, the biosynthetic/degradative enzyme(s) and/or cognate receptor(s) of the aforementioned lysophospholipids (S1P and lyso-PA) are pharmacological targets for drugs already in clinical use or under investigation in different phases of clinical trials for an array of human neurological and immunological disorders (Gardell et al., 2006; Yanagida and Valentine, 2020). Recently, the lysophosphatidylserines (lyso-PSs) have emerged as yet another important class of signaling lysophospholipids (Shanbhag et al., 2020), with

potent bioactivities in the mammalian central nervous and immune system.

Cellular pharmacological studies have shown that lyso-PSs regulate several immunological processes (Shanbhag et al., 2020) such as macrophage activation to clear apoptotic cells (Frasch and Bratton, 2012), mast cell degranulation (Lloret and Moreno, 1995), leukemic cell stimulation (Park et al., 2005), chemotaxis of human gliomas (Lee et al., 2008), and maturation of regulatory T cells (Barnes et al., 2015), and perhaps signal through Toll-like receptors (TLRs) (Van Der Kleij et al., 2002) and/or G-protein-coupled receptors (GPCRs) (Inoue et al., 2012) in the mammalian nervous and immune system. Interestingly, and of biomedical relevance, mutations to the putative lyso-PS receptors in humans have been linked to different autoimmune diseases (Szymanski et al., 2014; Napier et al., 2015; Chu et al., 2013). Murine studies have recently shown that accumulation of lyso-PS, especially very-long-chain (VLC) lyso-PSs (Blankman et al., 2013), in the mammalian brain is a major cause that drives the pathology of the early-onset human neurological disorder PHARC (polyneuropathy, hearing loss, ataxia, retinitis pigmentosa, and cataract) (Fiskerstrand et al., 2009, 2010).
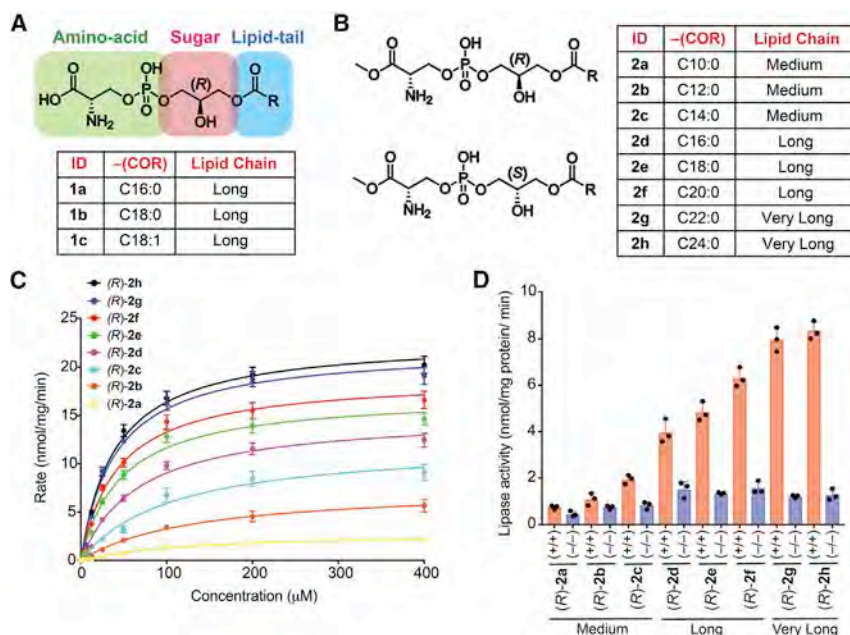
Figure 1. Structure of Me-lyso-PSs, and testing them as substrates against ABHD12

(A and B) The chemical structures of (A) commercially available canonical natural lyso-PSs and (B) our synthetic Me-lyso-PS lipid library with both (*R*)- and (*S*)-stereoisomers.

(C) Enzyme kinetic assays for membrane lysates (10 μg) of HEK293T cells transfected with hABHD12 tested against the (*R*)-Me-lyso-PSs (0–400 μM, 30 min, 37°C, n = 3/data point). The line connecting the points represents a fit to the Michaelis-Menten enzyme kinetics equation. See Table 1 for all enzyme kinetics parameters.

(D) Lipase assays for (*R*)-Me-lyso-PSs (100 μM, 30 min, 37°C, n = 3/group) tested against brain membrane lysates (20 μg) from wild-type (WT) (+/+) or ABHD12 knockout (−/−) mice. All data presented in (C) (data points) and (D) (bars) are presented as mean ± standard deviation (SD).

Interestingly, PHARC is caused by deleterious mutations to the *abhd12* gene (Fiskerstrand et al., 2009, 2010), which encodes an integral membrane metabolic serine hydrolase ABHD12 (α/β hydrolase domain-containing protein 12), a major and, to date, only *in vivo* functionally characterized lyso-PS lipase (Kamat et al., 2015; Blankman et al., 2013; Singh et al., 2020).

Given the strong link between lyso-PSs and human diseases, mechanistic studies are much needed to understand in more detail and biochemically characterize the signaling pathways influenced by lyso-PSs *in vivo*. Two factors complicate and/or limit such studies: (1) unlike other signaling lipids (e.g., S1P, 2-AG, AEA), *in vivo* lyso-PSs are found esterified with different fatty acids (ranging from medium-chain [C10] to VLC [C24]) (Blankman et al., 2013; Barnes et al., 2015), and hence the precise physiological contributions of the individual lyso-PSs remain cryptic; (2) commercially, lyso-PSs are limited, and even those that are available are esterified only with long-chain (LC) fatty acids (C16:0, C18:0, and C18:1) (Figure 1A). Therefore, delineating the biological contributions of medium or VLC lyso-PSs has not been possible to date.

To address the aforementioned problems, here we describe the synthesis of methyl esters of lyso-PS (Me-lyso-PS) bearing fatty acids of varying chain lengths ranging from medium-chain (C10–C14) to LC (C16–C20) to VLC (>C20) having the canonical natural (*R*)- or unnatural (*S*)-configuration at the glycerol backbone. Next, we test these synthetic Me-lyso-PS lipids in a variety of biological assays, and show that the canonical (*R*)-Me-lyso-PSs are highly bioactive while the corresponding unnatural (*S*)-Me-lyso-PSs are largely inactive. Specifically, we show that (*R*)-Me-lyso-PS are excellent substrates for the PHARC-associated lyso-PS lipase ABHD12, and confirm this enzyme's preference for VLC lyso-PS lipids (Joshi et al., 2018; Kamat et al., 2015; Blankman et al., 2013). Furthermore, we show that cellular carboxylesterases hydrolyze the methyl-ester moiety of Me-lyso-PSs to yield lyso-PSs, and thus demonstrate that the synthetic Me-lyso-PSs serve as stable prodrug-like biological precursors

to lyso-PSs. Of note, we report the distinct contribution of individual lyso-PS lipids in activation and pro-inflammatory responses from macrophages and in the release of histamine during mast cell degranulation, and specifically show how the fatty acid chain length of lyso-PSs plays a critical role in the output of the aforementioned important immunological processes. Finally, we also annotate the metabolic serine hydrolase ABHD12 as a major lyso-PS lipase in primary mast cells, and expand the possible physiological role of this biomedically important lipase to an additional immunological process.

RESULTS

Synthesis of Me-lyso-PS lipids

Structurally, lyso-PSs are composed of three building blocks: (1) a sugar backbone (glycerol), (2) an amino acid head group (phospho-L-serine), and (3) a lipid tail (fatty acid) (Figure 1A) (Fahy et al., 2011). It is this intricate combination of hydrophilic (glycerol and phospho-L-serine) and hydrophobic (fatty acid) biological building blocks that confers amphiphilic properties to lyso-PSs and enables them to access different cellular membranes, organelles, and compartments. Given this amphiphilic property, lyso-PSs serve as potent hormone-like mediators of various important immunological processes (Vance, 2015; Tracey et al., 2018; Shanbhag et al., 2020). From a stereochemical perspective, all natural lyso-PSs have two chiral centers: (1) α-carbon of the phospho-L-serine head group and (2) *sn-2* carbon of the (*R*)-glycerol backbone (Figure 1A) (Mallik et al., 2018). Biosynthetically, lyso-PSs are made from phosphatidylserine (PS) precursors, by the enzymatic action of PS-specific phospholipases (Hosono et al., 2001; Kamat et al., 2015), and subsequent studies have shown that physiologically, almost all lyso-PSs exists as 1-(fatty acyl)-2-hydroxy-*sn*-glycero-3-phospho-L-serine (Iwashita et al., 2009; Kamat et al., 2015). Given the synthetic challenges in making this bioactive lipid, for example, (1) combination of the aforementioned hydrophilic and hydrophobic moieties, (2) lipophilicity of the final molecule, and (3) the need for retention in configuration of the two chiral centers toward making the correct diastereomer,

Table 1. Kinetic constants for lyso-PS and Me-lyso-PS substrates tested against hABHD12 (HEK293T membrane lysates transiently transfected with hABHD12)

Lyso-PS species	Fatty acid chain length: unsaturation	V_{max} (nmol/mg protein/min)	K_M (µM)	V_{max}/K_M (nmol/mg protein/min/M) ($\times 10^5$)
1a	16:0	15.6 ± 0.6	72 ± 8	2.2 ± 0.3
1b	18:0	18.3 ± 0.5	48 ± 4	3.8 ± 0.4
1c	18:1	17.8 ± 0.6	46 ± 6	3.8 ± 0.5
(R)-**2a**	10:0	2.9 ± 0.2	126 ± 18	0.2 ± 0.04
(R)-**2b**	12:0	7.6 ± 0.3	131 ± 14	0.6 ± 0.06
(R)-**2c**	14:0	12.2 ± 0.6	106 ± 14	1.1 ± 0.1
(R)-**2d**	16:0	15.2 ± 0.6	67 ± 7	2.3 ± 0.3
(R)-**2e**	18:0	17.2 ± 0.6	47 ± 5	3.7 ± 0.5
(R)-**2f**	20:0	19.0 ± 0.6	43 ± 4	4.4 ± 0.5
(R)-**2g**	22:0	22.0 ± 0.6	40 ± 4	5.5 ± 0.6
(R)-**2h**	24:0	22.9 ± 0.6	40 ± 4	5.7 ± 0.6
(S)-**2a**	10:0	0.2 ± 0.02	275 ± 32	0.007 ± 0.001
(S)-**2b**	12:0	0.4 ± 0.05	255 ± 35	0.016 ± 0.002
(S)-**2c**	14:0	0.6 ± 0.1	215 ± 28	0.028 ± 0.003
(S)-**2d**	16:0	0.8 ± 0.1	187 ± 24	0.043 ± 0.006
(S)-**2e**	18:0	1.2 ± 0.1	178 ± 25	0.067 ± 0.008
(S)-**2f**	20:0	1.3 ± 0.2	165 ± 23	0.078 ± 0.009
(S)-**2g**	22:0	1.2 ± 0.2	167 ± 26	0.072 ± 0.009
(S)-**2h**	24:0	1.2 ± 0.3	176 ± 31	0.068 ± 0.008

only three naturally occurring LC lyso-PSs (**1a–1c**) are commercially available, thus limiting any rigorous structure-activity relationship (SAR) studies for this important lysophospholipid class (Figure 1A). Since the commercial paucity of lyso-PSs would impede our proposed studies, here we describe a facile synthesis route toward making Me-lyso-PS esterified with saturated fatty acids of varying chain lengths ranging from medium-chain to VLC (Figure 1B and Data S1). Speculating that the free reactive carboxylate moiety of the amino acid end of the molecule might cross-react and complicate the synthesis, we decided to make the Me-lyso-PS version. Our synthetic route successfully afforded the naturally occurring canonical (R)-Me-lyso-PSs (Figure 1B and Data S1) and the unnatural (S)-Me-lyso-PSs (Figure 1B and Data S1) with the same fatty acids (Figure 1B) to yield final compounds ((R)-**2a–2h** or (S)-**2a–2h**) in milligram quantities.

ABHD12 prefers VLC lyso-PSs as substrates

The lipids previously tested as substrates for the mammalian lyso-PS lipase ABHD12 have been commercially available LC lyso-PSs (**1a–1c**) (Blankman et al., 2013; Kamat et al., 2015) (Figure 1A) and various monoacylglycerol (MAG) lipids (Blankman et al., 2007; Joshi et al., 2018; Navia-Paldanius et al., 2012). In the absence of a commercial source for medium or VLC lyso-PSs, which to the best of our knowledge have not been tested against ABHD12, the MAG lipids have served as excellent surrogates for performing SAR studies toward biochemically understanding the substrate preference for this lipase (Joshi et al., 2018). Therefore, having synthesized the library of (R)- and (S)-Me-lyso-PSs containing medium-chain, LC, and VLC variants (nomenclature in Figure 1B), we first wanted to test whether these lipids were indeed substrates for ABHD12. Leveraging established liquid chromatography coupled with mass spectrom-

etry (LC-MS)-based substrate assays (Joshi et al., 2018), we found that both recombinant human ABHD12 (hABHD12) (Table 1 and Figure S1A) and endogenous mouse brain ABHD12 (mABHD12) (Figure S1B) robustly turned over (R)-Me-lyso-PSs, and for the same fatty acid, LC (R)-Me-lyso-PS and corresponding canonical natural LC lyso-PS behaved almost identically. Next, we performed rigorous enzyme kinetics measurements for our (R)-Me-lyso-PS library against hABHD12 (Figure 1C and Table 1) and found that hABHD12 strongly prefers VLC (R)-Me-lyso-PSs as substrates, with (R)-**2h** (C24:0, V_{max} = 22.9 ± 0.6 nmol/mg protein/min, K_M = 40 ± 4 µM) and (R)-**2g** (C22:0, V_{max} = 22.0 ± 0.6 nmol/mg protein/min, K_M = 40 ± 4 µM) being the best substrates. Furthermore, mouse brain membrane lysates were assayed against the same Me-lyso-PS library, and here too we found that mABHD12 strongly prefers VLC (R)-Me-lyso-PSs, with (R)-**2h** (C24:0, rate = 8.2 ± 0.3 nmol/mg protein/min) and (R)-**2g** (C22:0, rate = 8.0 ± 0.3 nmol/mg protein/min) being the best substrates (Figure 1D). In this experiment, mouse brain membrane lysates from ABHD12-null mice were used as controls to delineate specific contributions from mABHD12 (Figure 1D). In both these assays, we also tested (S)-Me-lyso-PSs and found, not surprisingly, that these were very poor substrates for hABHD12 (Table 1 and Figure S1C) and mABHD12 (Figure S1D), with catalytic efficiencies 100-fold lower than that of corresponding (R)-Me-lyso-PSs for hABHD12 (Table 1). Taken together, these substrate assays conclusively show that the ABHD12-catalyzed lyso-PS lipase reaction is highly stereospecific, prefers VLC (R)-lyso-PSs as substrates, and, together with recent findings (Singh et al., 2020; Joshi et al., 2018), now provides a concrete biochemical explanation as to why VLC lyso-PSs accumulate the most in ABHD12 knockout mouse brains (Blankman et al., 2013).
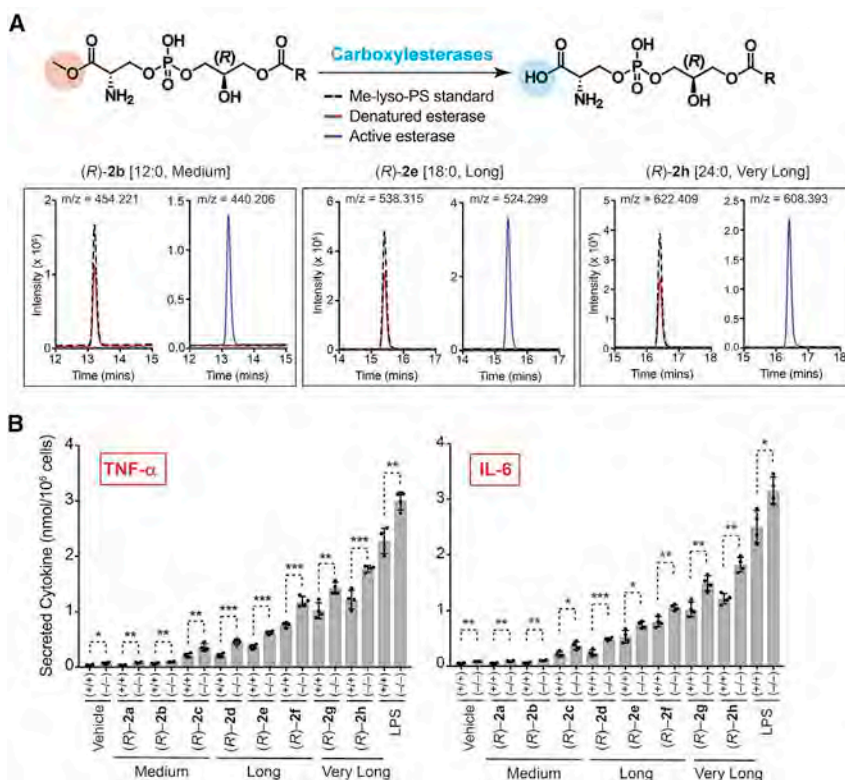
Figure 2. Metabolism of Me-lyso-PSs by carboxylesterases and the pro-inflammatory activity of Me-lyso-PSs in macrophages

(A) Top: the enzymatic reaction for metabolism (hydrolysis) of Me-lyso-PSs to the corresponding lyso-PSs catalyzed by carboxylesterases. Bottom: extracted ion chromatograms from a LC-MS analysis of (R)-**2b** (C12:0) ([M-H]⁻ = 454.221), (R)-**2e** (C18:0) ([M-H]⁻ = 538.315), and (R)-**2h** (C24:0) ([M-H]⁻ = 622.409) showing the complete conversion of the parent compound (Me-lyso-PS) to the corresponding lyso-PS (loss of 14 Da) following treatment with active (blue trace), but not denatured (red trace), porcine liver carboxylesterase (0.1 U, 15 min, 37°C). In these assays, 100 μg of the (R)-Me-lyso-PS was used, and a no-enzyme standard only control (dotted black trace) was also included for the same treatment. This LC-MS experiment was done twice for each of the (R)-Me-lyso-PS, with reproducible results each time.

(B) Secreted TNF-α and IL-6 from PPMs harvested from WT (+/+) or ABHD12 knockout (−/−) mice following treatment with vehicle (DMSO) or lipopolysaccharide (LPS) or (R)-**2a–2h** (1 μM, 4 h, 37°C); All data are presented as mean ± SD (n = 4/group). *p < 0.05, **p < 0.01, ***p < 0.001 versus (+/+) group by Student's two-tailed unpaired parametric t test.

Cellular carboxylesterases metabolize Me-lyso-PS to lyso-PS

Having synthesized Me-lyso-PSs, we postulated that these might be metabolized by cellular carboxylesterases to yield the corresponding lyso-PSs (Figure 2A). To test this hypothesis, we incubated three (R)-Me-lyso-PSs of varying lipid tails ((R)-**2b** [C12:0, medium-chain], (R)-**2e** [C18:0, LC], or (R)-**2b** [C24:0, VLC]) with active or denatured porcine liver carboxylesterase, and upon this treatment, by LC-MS (Joshi et al., 2018) we checked for the formation of the corresponding canonical lyso-PSs. We found for all the three (R)-Me-lyso-PSs subjected to this treatment that upon incubation with active but not the denatured carboxylesterase, the (R)-Me-lyso-PS was completely consumed and a new peak was observed with mass shift of ~14 Da (parent m/z − 14 Da) (Figure 2A). The mass of this new peak corresponds to the loss of the methyl group from (R)-Me-lyso-PS to yield the corresponding canonical (R)-lyso-PS via hydrolysis by the carboxylesterase (Figure 2A). Since we planned to test this synthetic Me-lyso-PS library for different biological activities in mammalian macrophages and mast cells, we decided to test whether lysates of these immune cells had carboxylesterases capable of converting (R)-Me-lyso-PSs to the canonical lyso-PSs. To negate any lyso-PS lipase type activity, we used active or denatured lysates from ABHD12-null primary peritoneal macrophages or peritoneal-derived cultured mast cells, and found that the active but not denatured lysates from both these immune cells converted the three previously tested (R)-Me-lyso-PSs, namely, (R)-**2b** (C12:0, medium-chain), (R)-**2e** (C18:0, LC), and (R)-**2h** (C24:0, VLC), to their corresponding canonical (R)-lyso-PS lipid (Figure S2A). Our results clearly show that cellular carboxylesterases

can hydrolyze the methyl group of (R)-Me-lyso-PSs to yield the corresponding canonical (R)-lyso-PSs (Figure 2A) and that the synthetic Me-lyso-PSs serve as stable prodrug-like biological surrogates to lyso-PSs, making them amenable to testing in primary macrophages and mast cells.

VLC lyso-PSs elicit robust pro-inflammatory responses in mammalian macrophages

Lyso-PSs have previously been shown to elicit immunological responses via pro-inflammatory cytokine secretion (e.g., tumor necrosis factor α [TNF-α], interleukin-6 [IL-6]) from mammalian macrophages (Kamat et al., 2015; Frasch and Bratton, 2012), and we wanted to assess whether the Me-lyso-PSs were capable of the same, having shown that carboxylesterases in primary macrophages can metabolize Me-lyso-PSs to lyso-PSs (Figure S2A). We found that when primary peritoneal macrophages (PPMs) isolated from wild-type (WT) mice were treated with equal concentrations of the canonical LC lyso-PSs (**1a** [C16:0] and **1b** [C18:0]) and the corresponding (R)-Me-lyso-PSs ((R)-**2d** and (R)-**2e**) of the same lipid tail, they secreted almost equal amounts of pro-inflammatory cytokines (TNF-α, IL-6) (Figure S2B). Not surprisingly, treating PPMs with unnatural (S)-Me-lyso-PSs (Figure S2C), corresponding free fatty acids (Figure S2C), or other lysophospholipids (lysophosphatidic acid [lyso-PA], lysophosphatidylglycerol [lyso-PG], and lysophosphatidylcholine [lyso-PC]) with same lipid tail (Figure S2D) failed to elicit any inflammatory response, suggesting that ligand recognition in PPMs in eliciting pro-inflammatory responses is highly stereospecific for (R)-lyso-PSs. Having established comparable bioactivities of canonical lyso-PSs and (R)-Me-lyso-PSs, we isolated PPMs from WT or ABHD12
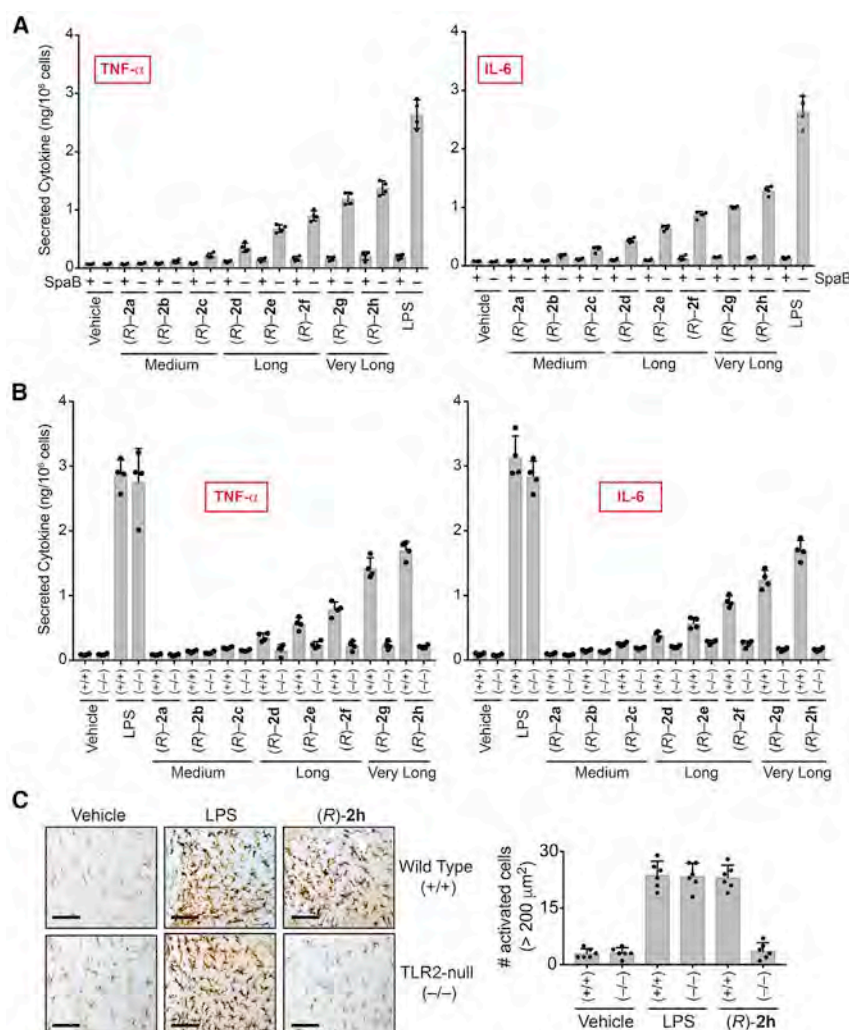
Figure 3. VLC lyso-PSs elicit pro-inflammatory responses via a TLR2-dependent pathway

(A and B) Secreted TNF-α and IL-6 from PPMs harvested from: (A) WT mice pre-treated with DMSO or SpaB (10 μM, 4 h, 37°C), followed by treatment with vehicle or LPS or (R)-**2a–2h** (1 μM, 4 h, 37°C); (B) WT (+/+) or TLR2 knockout (−/−) mice following treatment with vehicle or LPS or (R)-**2a–2h** (1 μM, 4 h, 37°C).

(C) Representative images from Iba-1 immunostaining for microglial activation (scale bars, 250 μm) and quantification of enlarged cells (>200 μm²) in the cerebellum (per 1.44 mm²) of WT (+/+) or TLR2 knockout (−/−) mice following intravenous injection of vehicle (PBS), LPS, or (R)-**2h** (C24:0) (all 1 mg/kg body weight, 10 h).

All data are presented as mean ± SD (n = 4–6/group).

macrophages (Figure 2B). We also performed a similar SAR study in human THP-1 macrophages and found similar results whereby VLC (R)-Me-lyso-PSs produced the highest secretion of pro-inflammatory cytokines (Figure S2E).

VLC lyso-PSs signal via TLR2 in mammalian macrophages

Reported literature speculates that VLC lyso-PSs perhaps signal through TLR2 (Van Der Kleij et al., 2002) although, to the best of our knowledge, VLC lyso-PSs have never been directly tested against any receptor for any immunological activity given their commercial unavailability. We found from a large-scale gene expression database (Figure S3A) (Wu et al., 2016) and by RT-PCR analysis (Figure S3B) that TLR2 (but none of the other putative lyso-PS receptors [Inoue et al., 2012]) is enriched on WT PPMs. Next, we found that pharmacological antagonism of TLR2 using Sparstolonin B (SpaB) (Liang et al., 2011) ablated the increased pro-inflammatory cytokine secretion caused by VLC (R)-Me-lyso-PS treatments in WT PPMs (Figure 3A), and in human THP-1 macrophages (Figure S2F). Here, we found that SpaB treatment also ablated the increased pro-inflammatory cytokine secretion caused by LPS treatment in WT PPMs (Figure 3A), consistent with SpaB's dual TLR2/TLR4 antagonism activity (Liang et al., 2011, 2013). Furthermore, we harvested PPMs from TLR2 knockout mice (Figure S3C) (Holla et al., 2016) and measured pro-inflammatory cytokine secretion following (R)-Me-lyso-PS treatments. Consistent with the pharmacological studies, we found that VLC (R)-Me-lyso-PSs, particularly (R)-**2g** and (R)-**2h**, produced highest secretion of TNF-α and IL-6 from WT PPMs, and this pro-inflammatory cytokine secretion was almost absent in TLR2-null PPMs (Figure 3B).

ABHD12 knockout mice display increased cerebellar microgliosis, whereby the accumulation of VLC lyso-PSs speculatively causes this neuroinflammatory phenotype (Blankman et al., 2013). To test whether VLC lyso-PSs indeed causes

knockout mice and incubated them with the (R)-Me-lyso-PS library to determine whether the length of lipid tail had any effect on pro-inflammatory cytokine secretion. Interestingly, we found from this SAR study that VLC (R)-Me-lyso-PSs, particularly (R)-**2g** (C22:0) and (R)-**2h** (C24:0), produced the highest pro-inflammatory cytokine secretion (TNF-α, IL-6) from WT PPMs (Figure 2B). Not surprisingly, ABHD12-null PPMs secreted significantly more pro-inflammatory cytokines compared with WT PPMs upon (R)-Me-lyso-PS treatments, consistent with their diminished lyso-PS lipase activity (Kamat et al., 2015) (Figure 2B). For either genotype, the pharmacological Me-lyso-PS treatments did not have any effect on cell viability.

Here, we used the bacterial outer membrane glycolipid lipopolysaccharide (LPS) as a positive control, as this endotoxin tested in PPMs mimics Gram-negative bacteria and robustly elicits immunological responses (pro-inflammatory cytokine secretion) in PPMs toward clearing this infection via a TLR4-dependent pathway (Raetz and Whitfield, 2002). In these assays, we found that the VLC (R)-Me-lyso-PS treatments produced ~60% pro-inflammatory cytokine secretion relative to similar LPS treatments in PPMs, suggesting that like LPS, VLC (R)-Me-lyso-PSs are potent immunological activators in mammalian
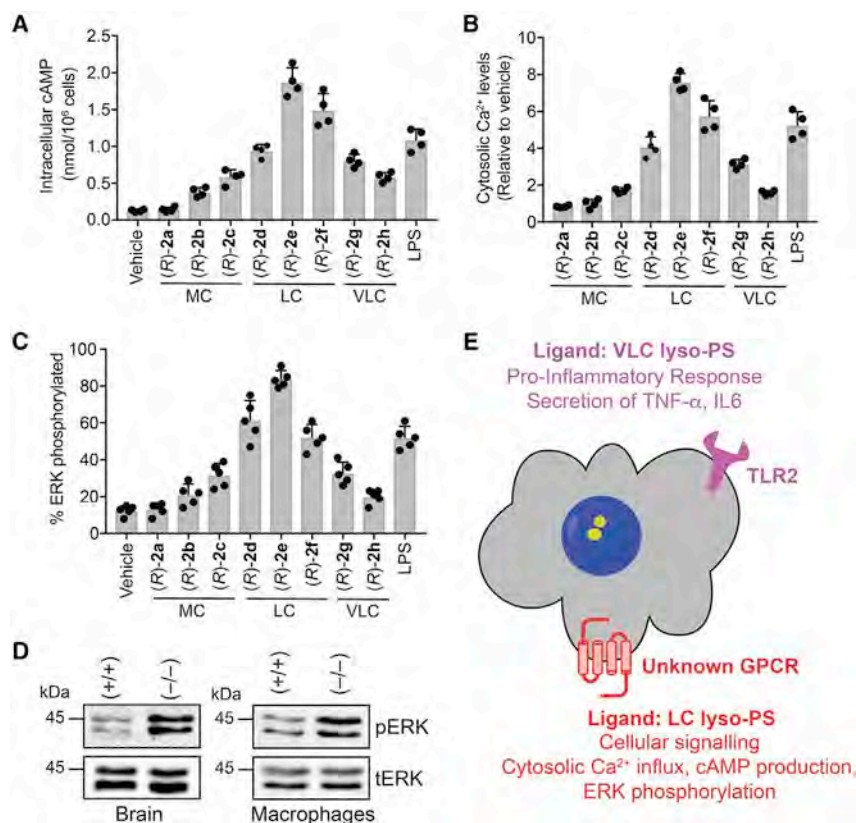
Figure 4. LC lyso-PSs activate macrophages through a putative GPCR

(A–C) (A) Intracellular cAMP, (B) relative cytosolic Ca^{2+} levels, and (C) percentage of phosphorylated ERK from WT PPMs following treatment with vehicle (DMSO) or LPS or (R)-**2a–2h** (1 μM, 10 min, 37°C). All data are presented as mean ± SD (n = 4–5/group), where MC denotes medium chain, LC long chain, and VLC very long chain.

(D) Representative western blots on lysates from brains (6-month-old mice) and LPS-treated (1 μM, 4 h, 37°C) PPMs harvested from WT (+/+) or ABHD12-null (−/−) mice, showing enhanced phosphorylation of ERK in both these tissues for the ABHD12-null (−/−) genotype.

(E) Schematic representation summarizing the lyso-PS signaling pathways by possibly two types of receptors on mammalian macrophages.

neuroinflammation and if they signal through TLR2, we intravenously injected a VLC (R)-Me-lyso-PS ((R)-**2h**, C24:0) into WT or TLR2-null mice, and quantified the extent of neuroinflammation by counting the number of activated microglia using an established immunohistochemical protocol (Singh et al., 2020; Blankman et al., 2013). We found that systemic administration of (R)-**2h** (C24:0) robustly induced cerebellar microgliosis in WT but not TLR2 knockout mice, suggesting that VLC (R)-Me-lyso-PSs signals through TLR2, causing neuroinflammation (Figures 3C and S4). As a positive control, we used LPS (which signals through TLR4) (Raetz and Whitfield, 2002) and intravenously injected it at the same dose and time, and found that the extent of neuroinflammation in WT and TLR2-null mice was almost identical (Figures 3C and S4). Furthermore, we found that relative to the positive control LPS, the VLC (R)-Me-lyso-PS (R)-**2h** (C24:0) produced comparable neuroinflammation (Figures 3C and S4). Interestingly, a LC (R)-Me-lyso-PS ((R)-**2e**, C18:0) intravenous injection for the same dosing regimen did not produce any neuroinflammation in WT mice (Figures S4A and S4B). Taken together, our results provide compelling *in vivo* evidence that VLC lyso-PSs (but not LC lyso-PSs) signal through TLR2, elicit a robust pro-inflammatory immune response, and are likely responsible for the neuroinflammation observed in ageing ABHD12 knockout mice, the murine model of PHARC (Blankman et al., 2013).

Mammalian macrophages have a cryptic lyso-PS receptor

Mammalian macrophages in response to lyso-PS produce increased intracellular cyclic adenosine 5′-monophosphate

(cAMP) (Sugita et al., 2013), cytosolic calcium (Ca^{2+}) influx (Park et al., 2005), and heightened phosphorylation of the nodal extracellular signal-regulated kinase (ERK) (Lee et al., 2008; Sugita et al., 2013), and we wanted to test whether Me-lyso-PSs also produce these phenotypes in mammalian macrophages. We found in WT PPMs that cellular cAMP (Figure 4A), relative cytosolic Ca^{2+} levels (Figure 4B), and ERK phosphorylation (Figure 4C) increased most profoundly upon treatment with LC (R)-Me-lyso-PSs, especially (R)-**2e** (C18:0), and that medium-chain or VLC (R)-Me-lyso-PS had negligible effects on these phenotypes. Surprisingly, the genetic deletion of TLR2 in PPMs (Figures S5A, S5B, and S6C) or its pharmacological antagonism in PPMs (Figures S5C, S5D, and S6B) and human THP-1 macrophages (Figures S5E, S5F, and S6B) showed no change on any of these phenotypes following (R)-Me-lyso-PS treatment. We also found that the LC (R)-Me-lyso-PSs (R)-**2e** (C18:0) and the corresponding canonical lyso-PS **1b** (C18:0) behaved identically in all these assays (Figures S6D–S6F). Not surprisingly, upon treating PPMs with (S)-Me-lyso-PSs (Figures S6A, S6E, and S6F), the corresponding free fatty acids or other lysophospholipids with lipid tail (C18:0) (Figures S6D–S6F), failed to elicit any significant response in any of these assays under similar treatment conditions, suggesting that these phenotypes in mammalian macrophages are specific to LC (R)-Me-lyso-PS (particularly C18:0). In all these assays, we found that the pharmacological Me-lyso-PS treatments did not affect cell viability.

Of note, brains and LPS-treated PPMs derived from ABHD12-null mice (where, in absolute concentrations, **1b** [C18:0 lyso-PS] is the most abundant, and significantly deregulated lyso-PS [Blankman et al., 2013; Kamat et al., 2015]) have markedly more ERK phosphorylation compared with WT control (Figure 4D). Given the heightened intracellular cAMP, cytosolic Ca^{2+} influx, phosphorylation of ERK, and inability of pharmacological antagonism or genetic disruption of TLR2 to affect any of these phenotypes, strongly supports the existence of another cryptic lyso-PS receptor on mammalian macrophages (in
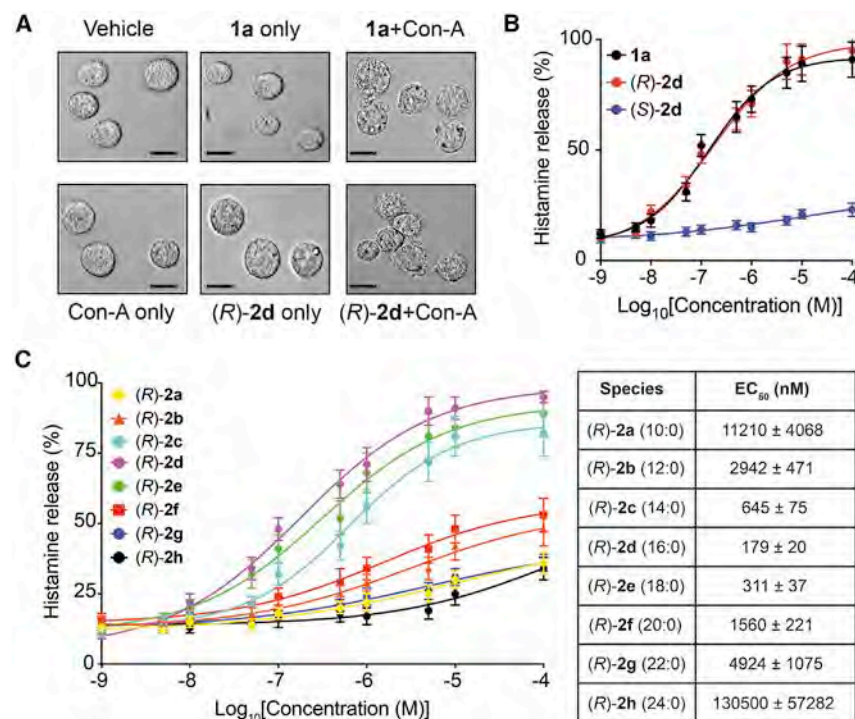
Figure 5. LC lyso-PSs robustly cause histamine release from primary mast cells

(A) Representative microscopy image showing degranulation of PCMCs after **1a** (C16:0 lyso-PS) or (R)-**2d** (C16:0) treatment (both 1 μM, 30 min, 37°C) in the presence of concanavalin A (Con-A). Scale bars, 100 μm.

(B) Histamine release profile from PCMCs treated with **1a** (C16:0 lyso-PS), (R)-**2d** (C16:0), or (S)-**2d** (C16:0) (1 nM to 10 mM, 30 min, 37°C, n = 3/data point).

(C) Dose-response and EC_{50} values for histamine release from PCMCs following treatment with the different (R)-Me-lyso-PSs (1 nM to 10 mM, 30 min, 37°C, n = 3/data point).

Species	EC_{50} (nM)
(R)-**2a** (10:0)	11210 ± 4068
(R)-**2b** (12:0)	2942 ± 471
(R)-**2c** (14:0)	645 ± 75
(R)-**2d** (16:0)	179 ± 20
(R)-**2e** (18:0)	311 ± 37
(R)-**2f** (20:0)	1560 ± 221
(R)-**2g** (22:0)	4924 ± 1075
(R)-**2h** (24:0)	130500 ± 57282

addition to TLR2) (Figure 4E). We speculate, based on aforementioned phenotypes, that this as yet unknown receptor is likely an unannotated GPCR (as putative lyso-PS GPCRs [Inoue et al., 2012] are absent in macrophages [Figures S3A and S3B]) that prefers LC lyso-PSs (particularly C18:0) as ligands to produce its downstream biological effects (Figure 4E).

LC lyso-PSs robustly induce mast cell degranulation

The release of histamine during mast cell degranulation is an extensively investigated lyso-PS-mediated immunological response (Sugo et al., 2006; Iwashita et al., 2009; Shanbhag et al., 2020), and yet contribution of individual lyso-PSs to this phenotype remain poorly understood. To address this, we generated peritoneal-derived cultured mast cells (PCMCs) (Meurer et al., 2016), and confirmed their ability to degranulate in the presence of **1a** (C16:0 lyso-PS) or the corresponding (R)-Me-lyso-PS, (R)-**2d** (C16:0) in the presence of concanavalin A (Con-A) (Figure 5A) (Iwashita et al., 2009; Sugo et al., 2006). Con-A is a well-characterized metalloprotein lectin of interest to immunologists, as it specifically binds mannosyl and/or glucosyl units of surface receptors of immune cells, and in doing so stabilizes receptor conformations that, in the context of PCMCs, facilitate lyso-PS-dependent histamine release (Lawson et al., 1978; Sullivan et al., 1975). Having shown their ability to degranulate, we quantitatively measured the histamine release from PCMCs using an established LC-MS method (Chimalakonda et al., 2015) (Figure S7). We found that the half-maximal effective concentration (EC_{50}) toward inducing histamine release during degranulation in PCMCs for **1a** (C16:0 lyso-PS, EC_{50} = 140 ± 22 nM) and (R)-**2d** (C16:0, EC_{50} = 179 ± 20 nM) were comparable, while the unnatural (S)-**2d** (C16:0, EC_{50} > 10 μM) failed to produce this phenotype (Figure 5B), suggesting that the putative re-

ceptor on PCMCs (likely GPR34 [Iwashita et al., 2009; Sugo et al., 2006; Ikubo et al., 2015], Figure S3A) is stereoselective in lyso-PS recognition. Next, we performed exhaustive dose-response studies with the (R)-Me-lyso-PS library and found that (R)-**2d** (C16:0, EC_{50} = 179 ± 20 nM) most potently induced histamine release during PCMC degranulation, with other LC (R)-Me-lyso-PSs (R)-**2e** (C18:0, EC_{50} = 311 ± 37 nM) and (R)-**2c** (C14:0, EC_{50} = 645 ± 75 nM) following suit (Figure 5C). This SAR study showed that medium-chain (<C12) or VLC (≥C20) (R)-Me-lyso-PSs failed to induce significant PCMC degranulation (EC_{50} > 2.5 μM) (Figure 5C), suggesting that besides the headgroup, the recognition of lipid tail is another major factor contributing to histamine release from mast cells during degranulation. In this SAR study, we found that the pharmacological Me-lyso-PS treatments had no effect on cell viability.

ABHD12 is the major lyso-PS lipase in primary mast cells

ABHD12 is a major lyso-PS lipase in different immune cells (Ogasawara et al., 2018; Kamat et al., 2015), but its biochemical function in primary mast cells remains unknown. Western blot analysis (Figure 6A) and diminished lyso-PS lipase activity (Figure 6B) confirmed the loss of ABHD12 in PCMCs derived from ABHD12-null mice. We also found that ABHD12-null PCMCs secreted significantly more lyso-PS (~2-fold more **1a** [C16:0] and **1b** [C18:0]) compared with WT PCMCs (Figure 6C). Given the diminished lyso-PS lipase activity, we postulated that **1a** (C16:0 lyso-PS) treatment would cause ABHD12-null PCMCs to degranulate at a lower dose of **1a**, and thereby release histamine more efficiently than WT PCMCs. Indeed, ABHD12-null PCMCs (EC_{50} = 47 ± 17 nM) released histamine more effectively than WT PCMCs (EC_{50} = 135 ± 32 nM) upon similar **1a** (C16:0 lyso-PS) treatment (Figure 6D). Finally, we measured serum histamine concentrations following intravenous (R)-**2d** (C16:0) injection in WT or ABHD12 knockout mice and found that ABHD12-null mice displayed heightened circulating histamine concentrations (~3-fold) compared with WT mice (Figure 6E). These results together confirm ABHD12's role as a major lyso-PS lipase in primary mast cells, where by regulating serum lyso-PS levels (Figure 6E) it controls systemic histamine release (Figure 6E).
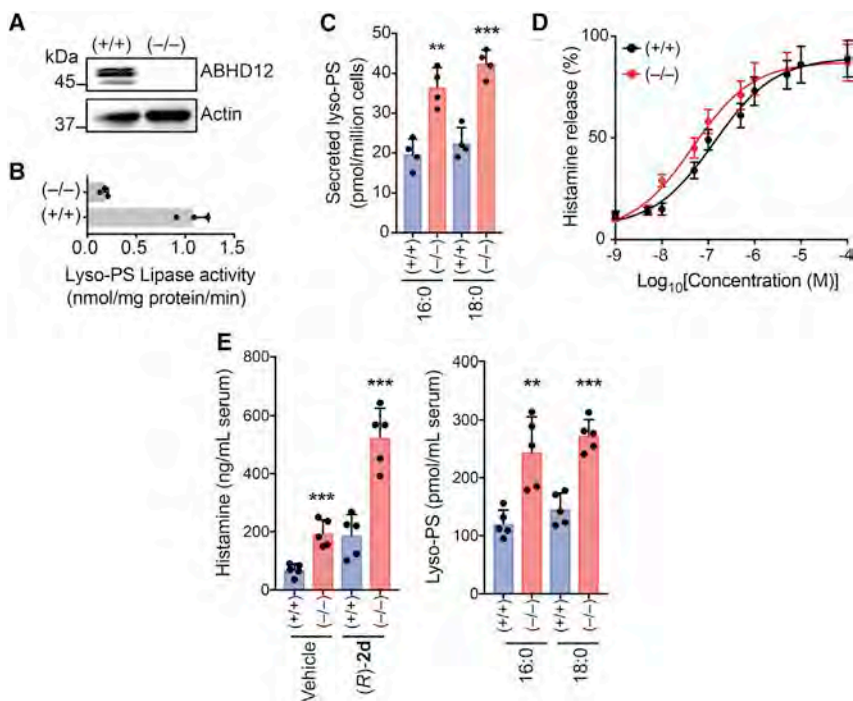
Figure 6. ABHD12 controls concentrations of LC lyso-PSs in primary mast cells, and thereby serum histamine levels

(A and B) (A) Representative western blot and (B) lyso-PS lipase activity assay (100 μM **1a** [C16:0 lyso-PS], 30 min, 37°C, n = 3/group), showing the loss of ABHD12 in PCMCs derived from ABHD12 knockout (−/−) mice.

(C) Concentrations of lyso-PS secreted from cultured PCMCs derived from WT (+/+) or ABHD12 knockout (−/−) mice, showing significantly increased **1a** (C16:0 lyso-PS) and **1b** (C18:0 lyso-PS) secretion from ABHD12-null PCMCs (n = 4/group).

(D) Histamine release profiles from PCMCs derived from WT (+/+) or ABHD12 knockout (−/−) mice treated with **1a** (C16:0 lyso-PS) (1 nM to 10 mM, 30 min, 37°C, n = 3/data point).

(E) Left: serum histamine levels in (+/+) or (−/−) mice following intravenous injections with vehicle (PBS) or (R)-**2d** (C16:0) (1 mg/kg, 2 h), showing increased serum histamine concentrations in the (−/−) mice compared with (+/+) controls for both treatments (n = 5/group). Interestingly, systemic administration of (R)-**2d** (C16:0) in (+/+) mice produces significantly more circulating serum histamine compared with the vehicle group, showing that (R)-**2d** (C16:0) by itself can induce histamine release from mast cells in *in vivo* settings. Right: serum lyso-PS concentrations in (+/+) or (−/−) mice, showing increased concentrations of circulating **1a** (C16:0 lyso-PS) and **1b** (C18:0 lyso-PS) in (−/−) mice, corroborating the increased serum histamine levels seen in these mice (n = 5/group). All data are presented as mean ± SD from at least n independent experiments. $**p < 0.01$, $***p < 0.001$ versus (+/+) group by Student's two-tailed unpaired parametric t test.

DISCUSSION

Signaling lipids are potent hormone-like biological molecules that regulate several important physiological processes in mammals, and their deregulation often has detrimental consequences that eventually manifest as disease in humans. Given their direct link to human diseases, the lyso-PSs have been recently emerged as yet another important class of signaling lipids (Shanbhag et al., 2020). However, unlike the established signaling lipids (e.g., 2-AG, AEA, S1P), *in vivo* lyso-PSs exist esterified with different lipid tails ranging from medium-chain (C10–C14) to LC (C16–C20) to VLC (>C20) fatty acids (Kamat et al., 2015; Blankman et al., 2013; Singh et al., 2020). Given the vast diversity in their *in vivo* content, it remains unclear as to which of these lyso-PSs have signaling functions and how they influence, regulate, and/or modulate different immunological processes. The lack of detailed SAR studies for these immunological phenotypes for lyso-PSs stems largely from the limited commercial availability and reported synthetic strategies toward making them, especially the medium-chain and VLC variants.

In this paper, we report the synthesis of Me-lyso-PSs having (R)- or (S)-stereochemistry at the *sn*-2 position of the glycerol backbone with varying lipid tails ranging from medium-chain to LC to VLC (Figure 1 and Data S1). Since the synthesis of lyso-PSs has proved challenging, and that of VLC lyso-PSs has not been reported to the best of our knowledge, our synthetic strategy allows the performance of rigorous SAR studies in diverse assays to delineate the specific function of the lipid tail in modulating a phenotype regulated by lyso-PSs. In all our biochemical and immunological assays, we find that (R)-Me-lyso-PSs serve as excellent bioequivalent surrogates for the canonical (R)-lyso-PSs, while the corresponding (S)-Me-lyso-PSs are biologically inactive. Since VLC lyso-PSs have never been tested against ABHD12, despite their accumulation in the brains of ABHD12-null mice (Blankman et al., 2013; Singh et al., 2020), here, by assaying the Me-lyso-PS library, we show conclusively that the ABHD12-catalyzed lyso-PS lipase reaction is stereoselective and prefers VLC lyso-PSs as substrates (Figure 1). Furthermore, we show through biochemical assays that the (R)-Me-lyso-PSs are acted upon by cellular carboxylesterases and converted to the corresponding canonical (R)-lyso-PSs, and that therefore, biologically, the (R)-Me-lyso-PSs function as prodrug-like surrogates for lyso-PSs in primary macrophages and mast cells (Figure 2).

Next, we wanted to understand the distinct role played by the lipid tail of individual lyso-PSs in the activation of macrophages and mast cell degranulation, as these immunological processes have been extensively studied and reported to be regulated by lyso-PSs (Shanbhag et al., 2020). In mammalian macrophages, we find that VLC Me-lyso-PSs produce the highest secretion of pro-inflammatory cytokines and that these pro-inflammatory responses are higher in ABHD12-null macrophages (Figure 2), given their diminished lyso-PS lipase activity (Kamat et al., 2015). Next, using pharmacological tools and genetic models, we show conclusively that VLC Me-lyso-PSs (but not LC lyso-PSs) orchestrate robust pro-inflammatory responses via a TLR2-dependent pathway to cause neuroinflammation (Figure 3). That VLC lyso-PSs signal through TLR2 and cause neuroinflammation (Figures 3 and S4) raises an intriguing possibility, corroborating a recent report (Ogasawara et al., 2018) that the

human neurological disease PHARC may itself be an autoimmune disease. Furthermore, we find that mammalian macrophages produce increased intracellular cAMP, cytosolic Ca^{2+} flux, and heightened ERK phosphorylation in response to LC lyso-PS treatments (particularly C18:0 lyso-PS) (Figure 4) via a TLR2-independent pathway (Figures S5 and S6), and we speculate that there is another cryptic receptor, likely a GPCR, that prefers LC lyso-PSs (particularly C18:0 lyso-PS) as ligands to produce these biological activities (Figure 4). We also show that LC lyso-PSs (especially C16:0 lyso-PS), but not medium-chain or VLC lyso-PSs, efficiently cause the release of histamine from mast cells during degranulation, suggesting that the putative lyso-PS receptor on mast cells (possibly GPR34 [Sugo et al., 2006]) prefers LC lyso-PSs (particularly C16:0 lyso-PS) as ligands to drive this immunological process (Figure 5). Finally, we report that ABHD12 is the major lyso-PS lipase in primary mast cells, where it controls the secreted lyso-PS levels, and its deletion in mice results in elevated levels of serum histamine and lyso-PS (Figure 6).

Projecting ahead, we propose that the functional antagonism of TLR2 might provide an excellent therapeutic paradigm in treating PHARC. This premise can be tested genetically by generating and characterizing ABHD12-TLR2 dual-knockout mice, and pharmacologically by discovering much needed *in vivo* active TLR2 functional antagonists. In addition, the annotation of ABHD12 as a major lyso-PS lipase in primary mast cells provides yet another avenue in understanding the immunomodulatory properties and the functional crosstalk of lyso-PSs between different immune cells particularly in the context of allergies and autoimmune conditions (Kelkar et al., 2019; Ogasawara et al., 2018). Finally, we would like to note that a major shortcoming of our study is the inability of our synthetic strategy in making Me-lyso-PSs with unsaturated fatty acid chains. Therefore, the development of such a synthetic methodology would enable making Me-lyso-PSs with unsaturated fatty acid chains and could also be leveraged to generate lyso-PS probes with suitable recently reported biorthogonal handles (Niphakis et al., 2015). Such bifunctional lyso-PS probes in tandem with advanced MS-based chemoproteomics platforms (Niphakis et al., 2015; Parker et al., 2017) will greatly facilitate the identification of hitherto unknown lyso-PS protein ligands and/or receptors, and this emerging knowledge will certainly expand our biological understanding of this underexplored immunomodulatory lipid class.

SIGNIFICANCE

Lysophospholipids are potent hormone-like biological mediators that regulate many important physiological processes in mammals. Recently, the lysophosphatidylserines (lyso-PSs) have emerged as yet another class of signaling lysophospholipids, with potent bioactivities in the central nervous and immune system in mammals, and deregulation in their metabolism has been linked to neurological and autoimmune disorders in humans. However, challenges in making lyso-PSs synthetically, and limited commercial sources for this lipid class, have greatly hampered any exhaustive structure-activity relationship (SAR) studies toward mechanistically understanding the role that lyso-PSs play in

different physiological processes. Here, we report a synthetic strategy toward making methyl esters of lyso-PSs (Me-lyso-PSs) with varying lipid tails, which serve as excellent prodrug-like biological surrogates for lyso-PSs, and focus on elucidating the role that the lipid tail of this lysophospholipid plays in regulating various immunological processes. Specifically, we study the lyso-PS-mediated activation of macrophages and mast cell degranulation processes, and show through detailed SAR studies that the lipid tail has profound effects on the phenotypical outputs of these important immunological processes. Our findings thus illuminate a physiological balance between long-chain and very-long-chain lyso-PSs, intricately regulated by the lyso-PS lipase ABHD12, and that disrupting this fine-tuned homeostasis results in immunological outputs that have detrimental pathological consequences in humans.

STAR★METHODS

Detailed methods are provided in the online version of this paper and include the following:

- KEY RESOURCES TABLE
- RESOURCE AVAILABILITY
  - Lead contact
  - Materials availability
  - Data and code availability
- EXPERIMENTAL MODEL AND SUBJECT DETAILS
  - Mice
  - Mammalian cell lines
- METHOD DETAILS
  - Reagents
  - Lyso-PS lipase substrate assays
  - Mammalian cells lipid treatments
  - Western blot analysis
  - ELISA assays
  - RT-PCR
  - Immunohistochemical analysis
  - Histamine estimation from mast cells
  - Lyso-PS measurements
  - Synthesis and compound characterization
- QUANTIFICATION AND STATISTICAL ANALYSIS

REFERENCES

Barnes, M.J., Li, C.M., Xu, Y., An, J., Huang, Y., and Cyster, J.G. (2015). The lysophosphatidylserine receptor GPR174 constrains regulatory T cell development and function. J. Exp. Med. *212*, 1011–1020.

Benjamini, Y., Krieger, A.M., and Yekutieli, D. (2006). Adaptive linear step-up procedures that control the false discovery rate. Biometrika *93*, 491–507.

Blankman, J.L., and Cravatt, B.F. (2013). Chemical probes of endocannabinoid metabolism. Pharmacol. Rev. *65*, 849–871.

Blankman, J.L., Long, J.Z., Trauger, S.A., Siuzdak, G., and Cravatt, B.F. (2013). ABHD12 controls brain lysophosphatidylserine pathways that are deregulated in a murine model of the neurodegenerative disease PHARC. Proc. Natl. Acad. Sci. U S A *110*, 1500–1505.

Blankman, J.L., Simon, G.M., and Cravatt, B.F. (2007). A comprehensive profile of brain enzymes that hydrolyze the endocannabinoid 2-arachidonoylglycerol. Chem. Biol. *14*, 1347–1356.

Chimalakonda, K.C., Pang, E., Weaver, J.L., Howard, K.E., Patel, V., and Boyne, M.T. (2015). Development and validation of a liquid-chromatography tandem mass spectrometry method to determine in vitro and in vivo histamine release. J. Pharm. Biomed. Anal. *102*, 494–499.

Chu, X., Shen, M., Xie, F., Miao, X.J., Shou, W.H., Liu, L., Yang, P.P., Bai, Y.N., Zhang, K.Y., Yang, L., et al. (2013). An X chromosome-wide association analysis identifies variants in GPR174 as a risk factor for Graves' disease. J. Med. Genet. *50*, 479–485.

Contos, J.J.A., Ishii, I., and Chun, J. (2000). Lysophosphatidic acid receptors. Mol. Pharm. *58*, 1188–1196.

Dennis, E.A. (2016). Lipidomics in disease and drug discovery. Faseb J. *30*, https://doi.org/10.1096/fasebj.30.1_supplement.114.3.

Dennis, E.A., and Norris, P.C. (2015). Eicosanoid storm in infection and inflammation. Nat. Rev. Immunol. *15*, 511–523.

Fahy, E., Cotter, D., Sud, M., and Subramaniam, S. (2011). Lipid classification, structures and tools. Biochim. Biophys. Acta *1811*, 637–647.

Fahy, E., Subramaniam, S., Brown, H.A., Glass, C.K., Merrill, A.H., Jr., Murphy, R.C., Raetz, C.R., Russell, D.W., Seyama, Y., Shaw, W., et al. (2005). A comprehensive classification system for lipids. J. Lipid Res. *46*, 839–861.

Fiskerstrand, T., H'mida-Ben Brahim, D., Johansson, S., M'zahem, A., Haukanes, B.I., Drouot, N., Zimmermann, J., Cole, A.J., Vedeler, C., Bredrup, C., et al. (2010). Mutations in ABHD12 cause the neurodegenerative disease PHARC: an inborn error of endocannabinoid metabolism. Am. J. Hum. Genet. *87*, 410–417.

Fiskerstrand, T., Knappskog, P., Majewski, J., Wanders, R.J., Boman, H., and Bindoff, L.A. (2009). A novel Refsum-like disorder that maps to chromosome 20. Neurology *72*, 20–27.

Fowler, C.J., Holt, S., Nilsson, O., Jonsson, K.O., Tiger, G., and Jacobsson, S.O. (2005). The endocannabinoid signaling system: pharmacological and therapeutic aspects. Pharmacol. Biochem. Behav. *81*, 248–262.

Frasch, S.C., and Bratton, D.L. (2012). Emerging roles for lysophosphatidylserine in resolution of inflammation. Prog. Lipid Res. *51*, 199–207.

Gardell, S.E., Dubin, A.E., and Chun, J. (2006). Emerging medicinal roles for lysophospholipid signaling. Trends Mol. Med. *12*, 65–75.

Gonzalez-Cabrera, P.J., Brown, S., Studer, S.M., and Rosen, H. (2014). S1P signaling: new therapies and opportunities. F1000prime Rep. *6*, 109.

Holla, S., Prakhar, P., Singh, V., Karnam, A., Mukherjee, T., Mahadik, K., Parikh, P., Singh, A., Rajmani, R.S., Ramachandra, S.G., and Balaji, K.N. (2016). MUSASHI-mediated expression of JMJD3, a H3K27me3 demethylase, is involved in foamy macrophage generation during mycobacterial infection. PLoS Pathog. *12*, e1005814.

Hosono, H., Aoki, J., Nagai, Y., Bandoh, K., Ishida, M., Taguchi, R., Arai, H., and Inoue, K. (2001). Phosphatidylserine-specific phospholipase A1 stimulates histamine release from rat peritoneal mast cells through production of 2-acyl-1-lysophosphatidylserine. J. Biol. Chem. *276*, 29664–29670.

Ikubo, M., Inoue, A., Nakamura, S., Jung, S.J., Sayama, M., Otani, Y., Uwamizu, A., Suzuki, K., Kishi, T., Shuto, A., et al. (2015). Structure-activity relationships of lysophosphatidylserine analogs as agonists of G-protein-coupled receptors GPR34, P2Y10, and GPR174. J. Med. Chem. *58*, 4204–4219.

Inoue, A., Ishiguro, J., Kitamura, H., Arima, N., Okutani, M., Shuto, A., Higashiyama, S., Ohwada, T., Arai, H., Makide, K., and Aoki, J. (2012). TGFalpha shedding assay: an accurate and versatile method for detecting GPCR activation. Nat. Methods *9*, 1021–1029.

Ishii, I., Fukushima, N., Ye, X., and Chun, J. (2004). Lysophospholipid receptors: signaling and biology. Annu. Rev. Biochem. *73*, 321–354.

Iwashita, M., Makide, K., Nonomura, T., Misumi, Y., Otani, Y., Ishida, M., Taguchi, R., Tsujimoto, M., Aoki, J., Arai, H., and Ohwada, T. (2009). Synthesis and evaluation of lysophosphatidylserine analogues as inducers of mast cell degranulation. Potent activities of lysophosphatidylthreonine and its 2-deoxy derivative. J. Med. Chem. *52*, 5837–5863.

Joshi, A., Shaikh, M., Singh, S., Rajendran, A., Mhetre, A., and Kamat, S.S. (2018). Biochemical characterization of the PHARC-associated serine hydrolase ABHD12 reveals its preference for very-long-chain lipids. J. Biol. Chem. *293*, 16953–16963.

Kamat, S.S., Camara, K., Parsons, W.H., Chen, D.H., Dix, M.M., Bird, T.D., Howell, A.R., and Cravatt, B.F. (2015). Immunomodulatory lysophosphatidylserines are regulated by ABHD16A and ABHD12 interplay. Nat. Chem. Biol. *11*, 164–171.

Kelkar, D.S., Ravikumar, G., Mehendale, N., Singh, S., Joshi, A., Sharma, A.K., Mhetre, A., Rajendran, A., Chakrapani, H., and Kamat, S.S. (2019). A chemical-genetic screen identifies ABHD12 as an oxidized-phosphatidylserine lipase. Nat. Chem. Biol. *15*, 169–178.

Kimura, I., Moritani, Y., and Tanizaki, Y. (1973). Basophils in bronchial asthma with reference to reagin-type allergy. Clin. Allergy *3*, 195–202.

Lawson, D., Fewtrell, C., and Raff, M.C. (1978). Localized mast cell degranulation induced by concanavalin A-Sepharose beads. Implications for the Ca2+ hypothesis of stimulus-secretion coupling. J. Cell Biol. *79*, 394–400.

Lee, S.Y., Lee, H.Y., Kim, S.D., Jo, S.H., Shim, J.W., Lee, H.J., Yun, J., and Bae, Y.S. (2008). Lysophosphatidylserine stimulates chemotactic migration in U87 human glioma cells. Biochem. Biophys. Res. Commun. *374*, 147–151.

Liang, Q.L., Wu, Q.A., Jiang, J.H., Duan, J.A., Wang, C., Smith, M.D., Lu, H., Wang, Q., Nagarkatti, P., and Fan, D.P. (2011). Characterization of Sparstolonin B, a Chinese herb-derived compound, as a selective toll-like receptor antagonist with potent anti-inflammatory properties. J. Biol. Chem. *286*, 26470–26479.

Liang, Q.L., Yu, F., Cui, X.D., Duan, J.A., Wu, Q.N., Nagarkatti, P., and Fan, D.P. (2013). Sparstolonin B suppresses lipopolysaccharide-induced inflammation in human umbilical vein endothelial cells. Arch. Pharmacal Res. *36*, 890–896.

Lloret, S., and Moreno, J.J. (1995). Ca^{2+} influx, phosphoinositide hydrolysis, and histamine release induced by lysophosphatidylserine in mast cells. J. Cell Physiol. *165*, 89–95.

Mallik, S., Prasad, R., Bhattacharya, A., and Sen, P. (2018). Synthesis of phosphatidylserine and its stereoisomers: their role in activation of blood coagulation. ACS Med. Chem. Lett. *9*, 434–439.

Meurer, S.K., Ness, M., Weiskirchen, S., Kim, P., Tag, C.G., Kauffmann, M., Huber, M., and Weiskirchen, R. (2016). Isolation of mature (peritoneum-derived) mast cells and immature (bone marrow-derived) mast cell precursors from mice. PLoS One *11*, e0158104.

Napier, C., Mitchell, A.L., Gan, E., Wilson, I., and Pearce, S.H.S. (2015). Role of the X-linked gene GPR174 in autoimmune Addison's disease. J. Clin. Endocrinol. Metab. *100*, E187–E190.

Navia-Paldanius, D., Savinainen, J.R., and Laitinen, J.T. (2012). Biochemical and pharmacological characterization of human alpha/beta-hydrolase domain containing 6 (ABHD6) and 12 (ABHD12). J. Lipid Res. *53*, 2413–2424.

Niphakis, M.J., Lum, K.M., Cognetta, A.B., 3rd, Correia, B.E., Ichu, T.A., Olucha, J., Brown, S.J., Kundu, S., Piscitelli, F., Rosen, H., and Cravatt, B.F. (2015). A global map of lipid-binding proteins and their ligandability in cells. Cell *161*, 1668–1680.

Ogasawara, D., Ichu, T.A., Vartabedian, V.F., Benthuysen, J., Jing, H., Reed, A., Ulanovskaya, O.A., Hulce, J.J., Roberts, A., Brown, S., et al. (2018). Selective blockade of the lyso-PS lipase ABHD12 stimulates immune responses in vivo. Nat. Chem. Biol. *14*, 1099–1108.

Park, K.S., Lee, H.Y., Kim, M.K., Shin, E.H., and Bae, Y.S. (2005). Lysophosphatidylserine stimulates leukemic cells but not normal leukocytes. Biochem. Biophys. Res. Commun. *333*, 353–358.

Parker, C.G., Galmozzi, A., Wang, Y., Correia, B.E., Sasaki, K., Joslyn, C.M., Kim, A.S., Cavallaro, C.L., Lawrence, R.M., Johnson, S.R., et al. (2017). Ligand and target discovery by fragment-based screening in human cells. Cell *168*, 527–541 e29.

Pathak, D., Mehendale, N., Singh, S., Mallik, R., and Kamat, S.S. (2018). Lipidomics suggests a new role for ceramide synthase in phagocytosis. ACS Chem. Biol. *13*, 2280–2287.

Raetz, C.R., and Whitfield, C. (2002). Lipopolysaccharide endotoxins. Annu. Rev. Biochem. *71*, 635–700.

Rajendran, A., Vaidya, K., Mendoza, J., Bridwell-Rabb, J., and Kamat, S.S. (2020). Functional annotation of ABHD14B, an orphan serine hydrolase enzyme. Biochemistry *59*, 183–196.

Rosen, H., Stevens, R.C., Hanson, M., Roberts, E., and Oldstone, M.B. (2013). Sphingosine-1-phosphate and its receptors: structure, signaling, and influence. Annu. Rev. Biochem. *82*, 637–662.

Rueden, C.T., Schindelin, J., Hiner, M.C., Dezonia, B.E., Walter, A.E., Arena, E.T., and Eliceiri, K.W. (2017). ImageJ2: ImageJ for the next generation of scientific image data. BMC Bioinformatics *18*, 529.

Schindelin, J., Rueden, C.T., Hiner, M.C., and Eliceiri, K.W. (2015). The ImageJ ecosystem: an open platform for biomedical image analysis. Mol. Reprod. Dev. *82*, 518–529.

Shanbhag, K., Mhetre, A., Khandelwal, N., and Kamat, S.S. (2020). The lysophosphatidylserines—an emerging class of signalling lysophospholipids. J. Membr. Biol. *253*, 381–397.

Singh, S., Joshi, A., and Kamat, S.S. (2020). Mapping the neuroanatomy of ABHD16A, ABHD12, and lysophosphatidylserines provides new insights into the pathophysiology of the human neurological disorder PHARC. Biochemistry *59*, 2299–2311.

Sugita, K., Yamamura, C., Tabata, K., and Fujita, N. (2013). Expression of orphan G-protein coupled receptor GPR174 in CHO cells induced morphological changes and proliferation delay via increasing intracellular cAMP. Biochem. Biophys. Res. Commun. *430*, 190–195.

Sugo, T., Tachimoto, H., Chikatsu, T., Murakami, Y., Kikukawa, Y., Sato, S., Kikuchi, K., Nagi, T., Harada, M., Ogi, K., et al. (2006). Identification of a lysophosphatidylserine receptor on mast cells. Biochem. Biophys. Res. Commun. *341*, 1078–1087.

Sullivan, T.J., Greene, W.C., and Parker, C.W. (1975). Concanavalin A-induced histamine release from normal rat mast cells. J. Immunol. *115*, 278–282.

Szymanski, K., Miskiewicz, P., Pirko, K., Jurecka-Lubieniecka, B., Kula, D., Hasse-Lazar, K., Krajewski, P., Bednarczuk, T., and Ploski, R. (2014). rs3827440, a nonsynonymous single nucleotide polymorphism within GPR174 gene in X chromosome, is associated with Graves' disease in Polish Caucasian population. Tissue Antigens *83*, 41–44.

Tracey, T.J., Steyn, F.J., Wolvetang, E.J., and Ngo, S.T. (2018). Neuronal lipid metabolism: multiple pathways driving functional outcomes in health and disease. Front. Mol. Neurosci. *11*, 10.

Van Der Kleij, D., Latz, E., Brouwers, J.F., Kruize, Y.C., Schmitz, M., Kurt-Jones, E.A., Espevik, T., De Jong, E.C., Kapsenberg, M.L., Golenbock, D.T., et al. (2002). A novel host-parasite lipid cross-talk. Schistosomal lyso-phosphatidylserine activates toll-like receptor 2 and affects immune polarization. J. Biol. Chem. *277*, 48122–48129.

Vance, J.E. (2015). Phospholipid synthesis and transport in mammalian cells. Traffic *16*, 1–18.

Wu, C., Jin, X., Tsueng, G., Afrasiabi, C., and Su, A.I. (2016). BioGPS: building your own mash-up of gene annotations and expression profiles. Nucleic Acids Res. *44*, D313–D316.

Wymann, M.P., and Schneiter, R. (2008). Lipid signalling in disease. Nat. Rev. Mol. Cell Biol. *9*, 162–176.

Yanagida, K., and Valentine, W.J. (2020). Druggable lysophospholipid signaling pathways. Adv. Exp. Med. Biol. *1274*, 137–176.

Kupyaphores are zinc homeostatic metallophores required for colonization of *Mycobacterium tuberculosis*

Kritee Mehdiratta[a,b], Shubham Singh[c], Sachin Sharma[d], Rashmi S. Bhosale[d], Rahul Choudhury[e] [ID], Dattatraya P. Masal[e] [ID], Alzu Manocha[d], Bhushan Dilip Dhamale[d], Naseem Khan[f], Vivekanand Asokachandran[a,b] [ID], Pooja Sharma[a,b], Melanie Ikeh[g,1], Amanda C. Brown[g,2], Tanya Parish[g,3] [ID], Anil K. Ojha[h,i] [ID], Joy Sarojini Michael[j], Mohammed Faruq[a,b], Guruprasad R. Medigeshi[f] [ID], Debasisa Mohanty[d], D. Srinivasa Reddy[e,4] [ID], Vivek T. Natarajan[a,b], Siddhesh S. Kamat[c,5] [ID], and Rajesh S. Gokhale[d,5,6]

[a]Council Of Scientific And Industrial Research–Institute of Genomics and Integrative Biology (CSIR-IGIB), New Delhi 110025, India; [b]Academy of Scientific and Innovative Research (AcSIR), Ghaziabad 201002, India; [c]Department of Biology, Indian Institute of Science Education and Research, Pashan, Pune 411008, India; [d]Immunometabolism Laboratory, National Institute of Immunology, New Delhi 110067, India; [e]CSIR–National Chemical Laboratory, Pune 411008, India; [f]Vaccine and Infectious Disease Research Center, Translational Health Science and Technology Institute, Faridabad 121001, India; [g]Barts & The London School of Medicine and Dentistry, Queen Mary University of London, London E1 2AT, United Kingdom; [h]Division of Genetics, Wadsworth Center, New York State Department of Health, Albany, NY 12208; [i]Department of Biomedical Sciences, School of Public Health, University at Albany, Albany, NY 12208; and [j]Department of Microbiology, Christian Medical College, Vellore 632004, India

Mycobacterium tuberculosis (*Mtb*) endures a combination of metal scarcity and toxicity throughout the human infection cycle, contributing to complex clinical manifestations. Pathogens counteract this paradoxical dysmetallostasis by producing specialized metal trafficking systems. Capture of extracellular metal by siderophores is a widely accepted mode of iron acquisition, and *Mtb* iron-chelating siderophores, mycobactin, have been known since 1965. Currently, it is not known whether *Mtb* produces zinc scavenging molecules. Here, we characterize low-molecular-weight zinc-binding compounds secreted and imported by *Mtb* for zinc acquisition. These molecules, termed kupyaphores, are produced by a 10.8 kbp biosynthetic cluster and consists of a dipeptide core of ornithine and phenylalaninol, where amino groups are acylated with isonitrile-containing fatty acyl chains. Kupyaphores are stringently regulated and support *Mtb* survival under both nutritional deprivation and intoxication conditions. A kupyaphore-deficient *Mtb* strain is unable to mobilize sufficient zinc and shows reduced fitness upon infection. We observed early induction of kupyaphores in *Mtb*-infected mice lungs after infection, and these metabolites disappeared after 2 wk. Furthermore, we identify an *Mtb*-encoded isonitrile hydratase, which can possibly mediate intracellular zinc release through covalent modification of the isonitrile group of kupyaphores. *Mtb* clinical strains also produce kupyaphores during early passages. Our study thus uncovers a previously unknown zinc acquisition strategy of *Mtb* that could modulate host–pathogen interactions and disease outcome.

zinc | metallophore | nutritional immunity | tuberculosis

Infection of humans by *Mycobacterium tuberculosis* (*Mtb*) has been the leading cause of mortality and morbidity for more than a century (1). This debilitating chronic pathogenesis is attributed to the ability of *Mtb* to manipulate and survive within the phagocytic cells of the immune system (2). *Mtb* colonization of macrophages initiates a competitive conflict for utilization of host nutrients, including elements such as iron, zinc, copper, magnesium, and selenium (3, 4). By limiting transition metal availability to invading pathogens, the host is known to restrict pathogen proliferation, a physiological concept called "nutritional immunity" (5). The pathogen endures through these early phases of adaptation by employing mechanisms that facilitate continual access to host micronutrient supply. Paradoxically, excess free metal ions can exert toxic effects on microbial survival. In fact, studies suggest that human macrophages intoxicate intracellular

Significance

Mycobacterium tuberculosis (*Mtb*) is the etiological agent of human tuberculosis (TB). *Mtb* can persist inside host macrophages by successfully adapting to intracellular conditions. Acquisition of balanced amounts of essential micronutrients is one such important process. Our studies have identified a metallophore produced on demand to restore *Mtb* zinc metabolic imbalance. These diacyl-diisonitrile lipopeptides, named kupyaphores, are specifically induced during infection and move in and out of cells to protect bacteria from host-mediated nutritional deprivation and intoxication. Furthermore, we identify an *Mtb* isonitrile hydratase homolog, expressed in low-zinc conditions, which probably facilitates zinc release from kupyaphores. Identification of this zinc acquisition strategy could provide opportunities in future to understand systemic zinc dysbiosis and associated manifestations in TB patients.

MICROBIOLOGY

Mtb with a burst of free zinc and copper (6–8). It is fascinating that these two strikingly opposing outcomes are resisted by intracellular pathogens like *Mtb* for the maintenance of zinc metallostasis.

The adaptive response strategy of bacterial pathogens to host-imposed zinc scarcity and poisoning is primarily governed by metal-sensing metalloregulatory proteins. As in most bacteria, *Mtb* contains two key zinc sensor proteins that coordinately function as uptake or efflux repressors. *Mtb* zinc uptake repressor (*zur*, Rv2359) regulates expression of several genes (9), including those involved in zinc uptake, while the efflux regulator (*zntR*, Rv3334) regulates transcription of genes encoding three types of exporters (10). *Mtb* has been shown to utilize P1-type ATPases to neutralize the toxic effects of zinc in macrophages (7). *Mtb* also employs zinc sparing to overcome zinc starvation, for example, remodeling of the ribosome 70S subunit (11). Similar mechanisms of metallostasis also govern the intracellular levels of iron during the host–pathogen interaction (12). In contrast, the general bacterial strategy of iron acquisition involving siderophore-mediated scavenging is yet to be recognized for other transition metals in *Mtb*. *Mtb* requirement of iron is accomplished by producing the siderophores—mycobactin and carboxymycobactin (13, 14). These siderophores move in and out of cells scavenging iron, releasing metal ions in the intracellular milieu, and then recycling the apo-siderophores. Ferric ion is released via reduction to ferrous ion or by modification of the siderophore scaffold using specific hydrolases (15). It is thus crucial to understand whether *Mtb* produces specialized iron siderophore-like small molecules on demand for zinc acquisition.

Staphylococcus aureus and *Pseudomonas aeruginosa* have been shown to produce staphylopine (16) and pseudopaline (17), respectively, for sequestering and importing metal ions, including zinc, from the host milieu to enhance the virulence and fitness of the intracellular bacteria (18). Although these molecules are not specific for zinc, opine-like metabolites have been referred to as zincophore and their biosynthesis is proposed to be widely distributed in bacteria (19). Recently, another class of low-molecular-weight metal chelating diisonitrile containing bacterial metabolites SF2768 and isonitrile lipopeptides have been identified from *Streptomyces thioluteus* and *Mycobacterium marinum*, respectively (20, 21). However, these metabolites could not be isolated from their natural hosts, but by heterologous overexpression of cognate biosynthetic gene clusters in host systems *Streptomycetes lividans* and *Escherichia coli*, respectively. The biosynthetic clusters of these diisonitrile-containing metabolites includes a nonribosomal peptide synthase (NRPS), fatty acyl-AMP ligase (FAAL), type II thioesterase, oxidoreductase and acyl carrier protein (ACP). Interestingly, a homologous five-gene biosynthetic cluster (Rv0097–Rv0101) can also be identified in the genome of *Mtb*, with the NRPS gene (Rv0101) being double the size (7,539 bp), as compared to other organisms. The mutant (Δ*nrps*) *Mtb* strain has been shown to grow at a lower rate in immunocompetent and immunocompromised mice, causing less lung pathology, and was associated with significantly increased mice survival rates (22). Despite the role of this biosynthetic cluster in *Mtb* virulence, the metabolite produced is not known. Moreover, the metabolic function as well as significance of this large 10.8 kbp genomic locus in tuberculosis (TB) pathophysiology remains to be elucidated.

In this study, we have isolated and characterized diacyl-diisonitrile lipopeptides, named kupyaphores, from human pathogen *Mtb*. Kupyaphores are stringently regulated and can move in and out of cells scavenging zinc to maintain bacterial fitness. These metallophores are biosynthesized on demand during early phases of *Mtb* infection and here we delineate pathophysiological relevance of kupyaphores in zinc mobilization and redistribution. Further, we identify an isonitrile

hydratase homolog in *Mtb* that is expressed in low-zinc conditions, and probably facilitates zinc release from these kupyaphores.

Results

Transcriptional Responses Maintain *Mtb* Zinc Homeostasis. Analysis of genomic loci of the cryptic biosynthetic cluster Rv0097–Rv0101 suggested classic zur-binding sites in the putative promotor regions, 61 bp upstream of Rv0096 and 354 bp upstream of Rv0099. Previous studies with zur-deleted *Mtb* strain did not show significant differential regulation for any of the genes from the Rv0097–Rv0101 cluster (9). Since these studies were carried out in the metal-rich Middlebrook 7H9 medium, we decided to examine mycobacterial transcriptional adaptive response at varying zinc conditions in the defined minimal Sauton's medium. The Middlebrook 7H9 medium used for culturing *Mtb* contains 6 μM concentration of ZnSO$_4$ and we performed wild-type *Mtb* (WT *Mtb*) growth kinetics at log-order lower and higher zinc concentrations. WT *Mtb* growth curves at 0.1 μM (low), 6 μM (optimal), and 50 μM (high) of zinc showed no significant differences (Fig. 1*A*). WT *Mtb* intracellular total zinc levels, as measured by inductively coupled plasma mass spectrometry (ICP-MS), were also similar for all three conditions (Fig. 1*B*).

Rv0099 is a member of a previously identified family of FAALs, and in the genomic context are found adjacent to polyketide synthases (PKS) or NRPS. All of these genomic clusters in *Mtb* produce virulent lipidic metabolites and show modest regulation at the transcriptional level (23, 24). With an anticipation to obtain a robust transcriptional response, we carried out five passages of WT *Mtb* in the minimal Sauton's medium treated with chelex X-100 resin (Fig. 1*C*). Adapted *Mtb* cells were then inoculated into low-, optimal-, and high-zinc conditions. RNA was isolated from log-phase cultures and transcriptome analysis was performed using an Illumina MiSeq sequencing platform for three biological replicates. After examining consistency of the raw reads (*SI Appendix*, Fig. S1*A*), we probed relatedness between these samples by using principal component analysis (*SI Appendix*, Fig. S1*B*). We observed tight clustering for all the three replicates of low- and high-zinc conditions, whereas one of the biological replicates showed greater variation from the optimal-zinc dataset.

To account for biological variation, we analyzed by including and excluding this dataset. This analysis yielded similar results for most of the significantly differentially expressed genes, many of which have been previously shown to be zinc (or metal) responsive genes. We compared differential expression analysis between 50 μM and 0.1 μM with cut off log$_2$ fold-change > 0.5 and false-discovery rate < 0.2 and visualized the data using an MA plot (Fig. 1*D*). This analysis identified a small set of 19 genes to be differentially regulated. Up-regulated genes included zinc transcription repressors *smtb* and *zur* (9) and efflux zinc pump *ctpC* (7), Rv2025c (25), and *cadI* (26). Genes belonging to the esx-1 and esx-3 export system showed highest down-regulation at both high- and low-zinc, when compared to optimal level of zinc. Previous study had suggested a role of these clusters in metal-dependent regulation (27). Of the FAAL-PKS/NRPS gene clusters, some of the genes belonging to mycobactin, pthiocerol dimycocerosate and the biosynthetic cluster Rv0097–Rv0101, showed modest up-regulation at both low- and high-zinc conditions (*SI Appendix*, Fig. S1*C*). Expression changes of the genes from Rv0097 to Rv0101 were corroborated by carrying out qRT-PCR analysis. We observed statistically significant up-regulation for four of five genes at both low- and high-zinc conditions, when compared with optimal conditions (Fig. 1*E*). We therefore hypothesized that this cluster may have involvement in *Mtb* zinc metallostasis.
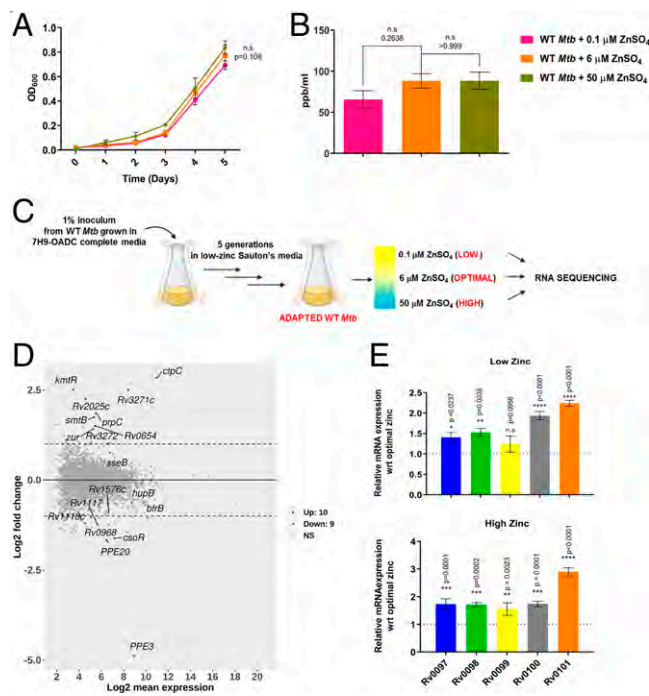
Fig. 1. *Mtb* transcriptional responses maintains zinc homeostasis. (*A*) Growth kinetics of WT *Mtb* grown in chelated Sauton's medium supplemented with varying zinc concentrations: 0.1 μM, 6 μM, and 50 μM. (*B*) ICP-MS analysis of total intracellular zinc content of *Mtb* grown in these three conditions. (*C*) Experimental design for generation of low-metal adapted WT *Mtb* strain. (*D*) MA plot of differential gene expression analysis in a 50 μM zinc supplemented condition as compared to 0.1 μM zinc supplementation with $\log_2$ fold-change > 0.5 and false-discovery rate < 0.2 as cutoff. Genes marked in red are significantly up-regulated, while genes marked in blue are significantly down-regulated. (*E*) Gene-expression analysis of Rv0097–Rv0101 through qRT-PCR under low- and high-zinc conditions as compared to optimal zinc concentration. Data represent mean ± SEM (*n* = 3 biological replicates), *P* value indicated for each data point.

Significance of *Mtb* nrps in Mycobacterial Physiology. *Mtb* gene cluster Rv0097–Rv0101 spans 10.8 kbp, which over the years has been implicated in *Mtb* virulence, without exactly delineating the biochemical function (22, 28, 29). The largest open reading frame (Rv0101) of the Rv0097–Rv0101 gene cluster codes for a bimodular NRPS. We generated a NRPS knockout strain in *Mtb* (Δ*nrps*) to assess the role of this gene cluster in metal homeostasis (*SI Appendix*, Fig. S2*A*). The mutant strain showed no growth profile differences under planktonic conditions in the 7H9 medium (*SI Appendix*, Fig. S2*B*). However, the Δ*nrps Mtb* mutant exhibited differences under biofilm growth conditions as reported earlier, and formed a fragile film lacking the characteristic reticulation of WT *Mtb* biofilms (29). This mutant phenotype could be reversed on complementation with an integrative shuttle cosmid vector containing an *Mtb* H37Rv fragment spanning Rv0096 to Rv0109 (*SI Appendix*, Fig. S2 *C* and *D*). We then examined the growth profiles of WT *Mtb* and Δ*nrps* strains in the metal-limited chelated Sauton's medium. The *Mtb* Δ*nrps* strain displayed defective growth in the Sauton's medium, which contains only glycerol and asparagine as sole carbon and nitrogen sources. We then examined the rescue of this growth defect by adding various divalent metals one at a time at 6 μM concentration. Δ*nrps* growth could be restored only upon zinc supplementation to Sauton's medium and no reversal in growth phenotype could be obtained for other metals, such as copper, magnesium, manganese, and iron (Fig. 2*A*).

We then evaluated growth of WT, the Δ*nrps* mutant, and the complemented strain (Δ*nrps:nrps*) at conditions of both low-

(Fig. 2*B*) and high-zinc (Fig. 2*C*) levels. While the Δ*nrps Mtb* mutant showed significantly reduced growth under both of these conditions, the complemented strain showed growth kinetics similar to WT *Mtb*. To understand whether the mutant strain had disrupted metal homeostasis, we measured metal ion concentrations within *Mtb* cells by using ICP-MS. At low-zinc conditions, the Δ*nrps* mutant strain showed a significant decrease in zinc levels (Fig. 2*D*), whereas zinc accumulation could be observed at high-zinc conditions (Fig. 2*E*). The complemented *Mtb* strain (Δ*nrps:nrps*) profiles were similar to WT cells. There was slight difference for copper levels between the mutant and WT (*SI Appendix*, Fig. S2*E*), and other metals—such as magnesium, cobalt, nickel, and manganese—showed no significant change across all three *Mtb* strains.

To understand the significance of the Rv0097–Rv0101 biosynthetic cluster in the context of *Mtb* pathogenesis, ex vivo infection experiments were performed with an immortalized murine bone marrow–derived RAW 264.7 macrophage cell line with WT and Δ*nrps Mtb* strains. Within 2 h of infection, remarkable up-regulation of the Rv0097–Rv0101 gene cluster could be noted in WT *Mtb* cells (*SI Appendix*, Fig. S3*A*). This up-regulation response dampens in 24 h in the macrophage infection assays, suggesting an early role of the Rv0097–Rv0101 cluster during *Mtb* infection. Furthermore, the intracellular free-zinc levels for WT, Δ*nrps* and complemented *Mtb* were measured using FluoZin 3-AM (FZ3-AM) dye, a zinc-selective indicator, 2 h postinfection. To observe *Mtb* cells in a fluorescence microscope, all the three strains were transformed with plasmid expressing mCherry. Macrophages infected with WT *Mtb* showed increased punctate signals for free-zinc, as compared with uninfected cells (Fig. 3*A*). Surprisingly, weak free-zinc signals could be observed in the mutant-infected macrophages, as measured by FZ3-AM. The complemented strain (Δ*nrps:nrps*) showed similar free-zinc levels to the WT *Mtb* strain as quantitated by confocal microscopy (Fig. 3*B*). Interestingly, almost all WT *Mtb* cells colocalized with free-zinc, as reported earlier (7).

To further understand these changes in zinc dynamics upon infection, we compared the zinc pools of macrophages and bacteria by performing differential lysis of WT and Δ*nrps* infected cells. The total zinc levels were then measured by ICP-MS analysis. The total zinc levels of either of the infected macrophages (WT or Δ*nrps Mtb*) were found to be comparable to uninfected macrophages (*SI Appendix*, Fig. S3*B*). Analysis of the total zinc pools of the internalized *Mtb*, however, interestingly revealed the zinc levels to be significantly low in Δ*nrps* as compared to WT *Mtb* (*SI Appendix*, Fig. S3*C*). No significant difference could be observed between the two strains for any other metal ion (*SI Appendix*, Fig. S3 *D* and *E*). Together, the induction of Rv0097–Rv0101 biosynthetic pathway and altered intracellular zinc concentration in Δ*nrps Mtb* strain provide evidence for the involvement of the unknown metabolite produced by this cryptic gene cluster in maintenance of bacterial zinc homeostasis.

Computational and Biochemical Analysis of *Mtb* nrps Biosynthetic Gene Cluster. To predict the metabolite produced by the biosynthetic operon Rv0097–Rv0101, we carried out detailed in silico analysis and also confirmed biochemical functions for three enzymes by performing in vitro assays. Retro-biosynthetic analysis based on previous studies suggested a putative pathway wherein FAAL10 (Rv0099) activates α/β unsaturated long-chain fatty acids to corresponding acyl-adenylates, which are then transferred onto the thiol group of phosphopantetheine group of ACP (Rv0100) protein (30, 31). This ACP-bound lipid chain can be modified by Rv0097 and Rv0098, as shown previously (21, 32). *Mtb* NRPS (Rv0101) contains two modules (bimodular), each consisting of three enzymatic domains:
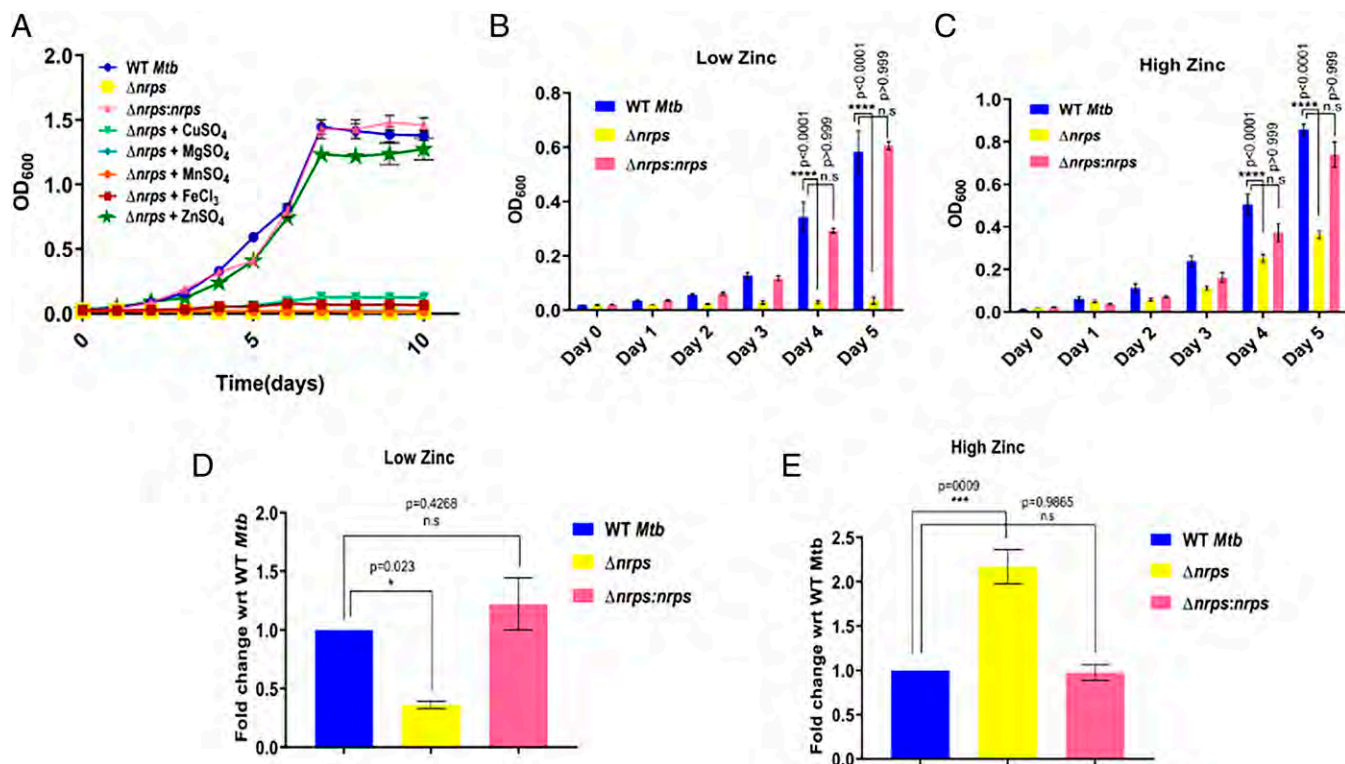
Mehdiratta et al.
Kupyaphores are zinc homeostatic metallophores required for colonization of *Mycobacterium tuberculosis*

PNAS | 3 of 12
https://doi.org/10.1073/pnas.2110293119

Fig. 2. Role of *Mtb nrps* in mycobacterial physiology. (*A*) Growth kinetics of WT and Δ*nrps* show mutant to be severely compromised in a nutrient-deficient condition of chelated Sauton's medium. Addition of other key transition elements—copper, magnesium, manganese, or iron—to Sauton's medium failed to revive mutant significantly. Only supplementation with 6 μM zinc could restore growth profile of Δ*nrps* strain. (*B* and *C*) Titration of Sauton's medium with different concentrations of zinc show compromised growth pattern of Δ*nrps* under both low- (0.1 μM) and high- (50 μM) zinc concentrations as compared to WT *Mtb*. Complementation of Δ*nrps* strain with a WT copy (Δ*nrps:nrps*) reversed the phenotype. (*D* and *E*) ICP-MS analysis of WT, Δ*nrps*, and Δ*nrps:nrps Mtb* strains to measure intracellular levels of total zinc under low- and high-zinc conditions. Data represent mean ± SEM (*n* = 3 biological replicates) with *P* values indicated for each data point.

condensation (C), adenylation (A), and thiolation (T) (33, 34). The second module of this NRPS protein contains a reductase (R) domain, which releases thioester-bound lipopeptides as corresponding alcohols (35) (Fig. 4*A*). Protein sequence analysis of the two modules of NRPS revealed the two C domains (C1 and C2) shows weak sequence homology (similarity/identity, 35/36%).

Recently, genome mining studies have revealed similar five-gene clusters from various *Actinomycetes* (20). We performed dendrogram-based analysis of C domains from NRPS proteins (unimodular or bimodular) of these five-gene clusters along with other atypical C domains. This analysis divided the C domains into two discrete clusters (*SI Appendix*, Fig. S4*A*), indicating that they may have distinctive catalytic functions. Interestingly, C2 domains from the bimodular NRPS clustered along with the typical C domains, whereas C1 domains formed a separate branch. Though both the domains are of similar length and share the conserved catalytic HHXXXDG motif, structural modeling of C1 domains show substantial homology to CoA-dependent acyltransferases. All C1 domains show unique conservation of amino acid residues around the active site pocket, suggestive of functional divergence from the cognate C domains (*SI Appendix*, Fig. S4 *B* and *C*) and we therefore refer to these as C1*. Based on reported studies of metabolites isolated from the heterologous overexpression systems for *M. marinum* and *S. thioluteus* (20, 21), we reasoned that this unusual C1* domain may be involved in the transfer of acyl chains on both the α-amino and ε-amino groups of a lysine.

To corroborate our computational prediction, we performed biochemical reconstitution of Rv0097 and Rv0098. Our previous

studies showed FAAL10 (Rv0099) to activate long-chain fatty acids as acyl-adenylates and transfer them onto the thiol group of phosphopantetheine ACP (Rv0100) protein (35). We confirmed similar activity for α/β unsaturated long-chain fatty acids. We cloned and expressed Rv0097 and Rv0098 in *E. coli* and purified the proteins using affinity chromatography. Enzymatic assays were then performed by using phosphopantetheine mimics, *N*-acetyl cysteamine (NAC) thioesters of α/β unsaturated fatty acids of different carbon lengths: C4, C8, and C12 (Fig. 4*B* and *SI Appendix*, Fig. S5). Enzymatic activities were confirmed using liquid chromatography coupled to mass spectrometry (LC-MS) assay protocols (36, 37). Addition of glycine to NAC-thioester of dodecenoic acid in the presence of enzyme Rv0098 identified a molecular ion peak at *m/z* of 374.2239, corresponding to Michael addition of glycine across unsaturated fatty acyl thioester. MS/MS analysis of this ion resulted in fragment ions of *m/z* [M-H]⁻ = 254.176, 74.025, and 58.030, providing confidence to the structure (Fig. 4*C*). Mass peak with *m/z* [M-H]⁻ = 265.192 probably corresponds to the hydrated form of the fragment ion of *m/z* = 248.0831. No activity was observed for NAC-thioester of crotonoic and minor products were obtained with octenoic acids. When the purified protein Rv0097 was included in the above assays, a new peak corresponding to *m/z* of 326.2085 could be observed in high-resolution LC-MS (LC-HRMS). This molecular ion, along with fragment ions, corresponded to the isonitrile modification of the of C12 fatty acyl-SNAC moiety (Fig. 4*D*). Such an isonitrile modified C12 ACP-bound acyl chain could then condense with first amino acid, which is selected by the adenylation domain of the first module of the NRPS protein (C1*-A1-T1). Computational algorithms predict the adenylation
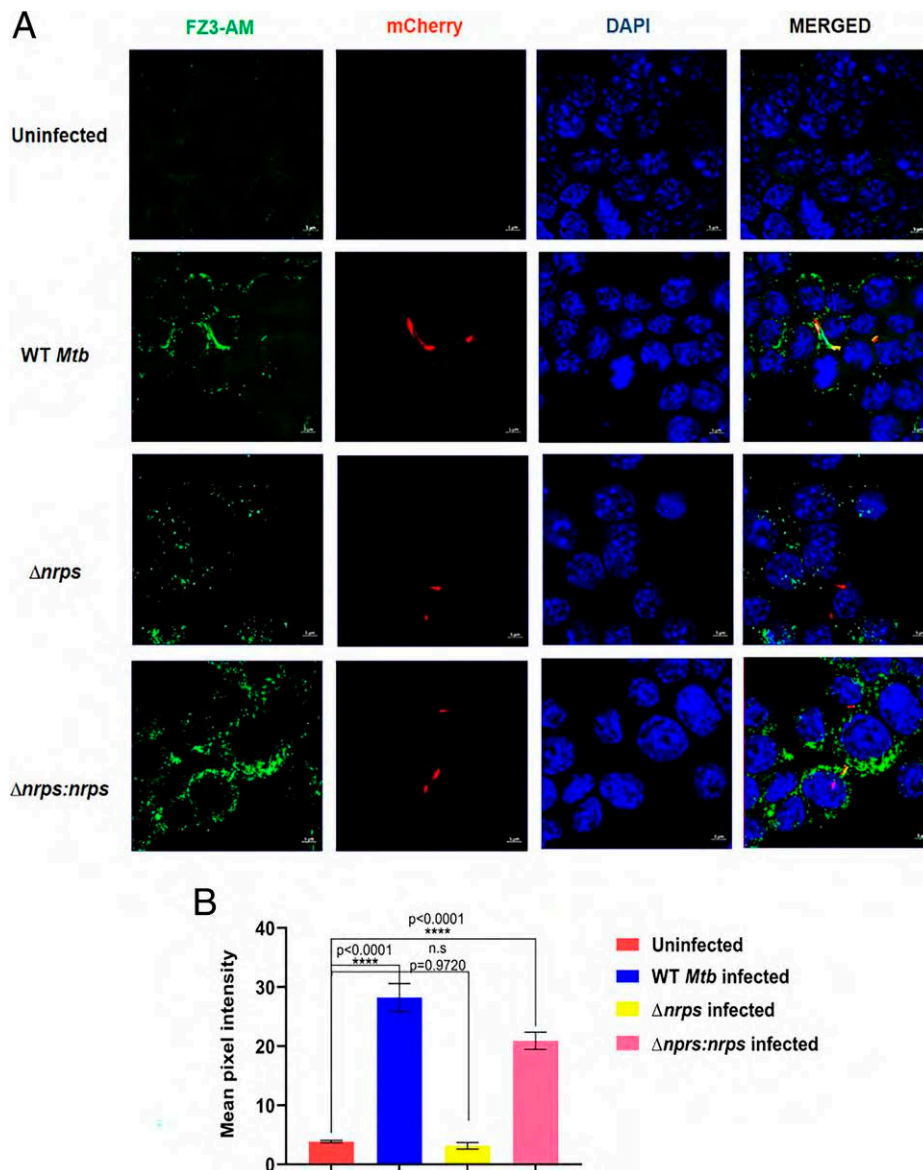
Mehdiratta et al.
Kupyaphores are zinc homeostatic metallophores required for colonization
of *Mycobacterium tuberculosis*

A

FZ3-AM | mCherry | DAPI | MERGED

Uninfected

WT *Mtb*

Δ*nrps*

Δ*nrps:nrps*

B

- Uninfected
- WT *Mtb* infected
- Δ*nrps* infected
- Δ*nprs:nrps* infected

Fig. 3. *Mtb nrps* modulates host free-zinc dynamics. (*A*) Free-zinc labeling using FZ3-AM dye for uninfected, mCherry-labeled WT, Δ*nrps*, and Δ*nrps:nrps Mtb* strains infected murine macrophages 2 h postinfection. (*B*) FZ3-AM signal quantitation from 75 cells for each condition. Unlike WT and Δ*nrps:nrps*-infected macrophages, Δ*nrps*-infected macrophages do not show elevated free-zinc levels as compared to uninfected macrophage. Data represent mean ± SEM (n = 3 biological replicates) with P values indicated for each data point.

A1 to activate lysine, while the second A2 domain shows specificity for phenylalanine (38, 39). Finally, the acyl chain would be reductively released to the corresponding alcohol, thus producing a novel isonitrile lipopeptide.

Identification and Characterization of Diacyl-Diisonitrile Lipopetides from Mtb. In order to isolate these molecules from *Mtb*, we extracted metabolites from *Mtb* cells grown in Middlebrook 7H9 medium and from biofilm using ethyl acetate. These samples were analyzed by LC-MS/MS using a recently developed method from our laboratory (36). Analysis of *Mtb* biofilm extract detected a cluster of unique peaks with m/z 707.5350, 721.5506, 735.5663, 763.5967, 833.6758, 847.6915, and 861.7071, which were absent in the *Mtb* planktonic cultures grown in Middlebrook 7H9 medium (Fig. 5*A*). The parent ion masses (**I–VII**) differed by a multiple of 14, typical of series with varying –CH$_2$ group and thus can be attributed to different acyl chain lengths. The previously reported molecular formula C$_{40}$H$_{73}$N$_6$O$_5$ with m/z of 717.5612 was absent in our biofilm-analyzed samples (29). MS/MS fragmentation patterns of parent ions revealed a common set of fragments with m/z values of [M+H]$^+$ 266.1863, 152.1080, 133.099, and 89.1073 (Fig. 5*B*). The m/z of 266.1863 along with the fragments of m/z

152.1080 and 133.099 can be assigned to phenylalaninol ion and ornithine ion, respectively. A peak of 89.1073 corresponds to decarboxylation of the ornithine ion, which suggests the backbone to be composed of a common core of ornithine and phenylalaninol dipeptide. Concomitantly, these peaks were absent in the biofilm metabolic extract of Δ*nrps* but could be detected in the Δ*nrps:nrps* strain (*SI Appendix*, Fig. S6*A*). Additionally, negative ion mode LC-MS analysis of the biofilm extract revealed two types of metabolites: symmetric (with identical acyl chains on the two –NH$_2$ groups of ornithine) and asymmetric (with different acyl chains on the two –NH$_2$ groups of ornithine) (*SI Appendix*, Fig. S6 *B* and *C*). Recently, click chemistry-based analytical detection of isonitrile using tetrazine has been reported (40). Tetrazine treatment of WT *Mtb* biofilm extract rapidly changed the color from pink to yellow (Fig. 5*C*) and the signals from MS analysis corresponding to **I–VII** diminished substantially (*SI Appendix*, Fig. S6*D*). Furthermore, the universal reaction product Py-aminepyrazoles with m/z [M+H]$^+$= 238.1014 could be detected only in the tetrazine-treated samples (Fig. 5*D*).

Furthermore, to confirm the isonitrile moiety and the overall chemical structure of the metabolite, we synthesized an analog of C18 lipopeptide with amine functionality at the β
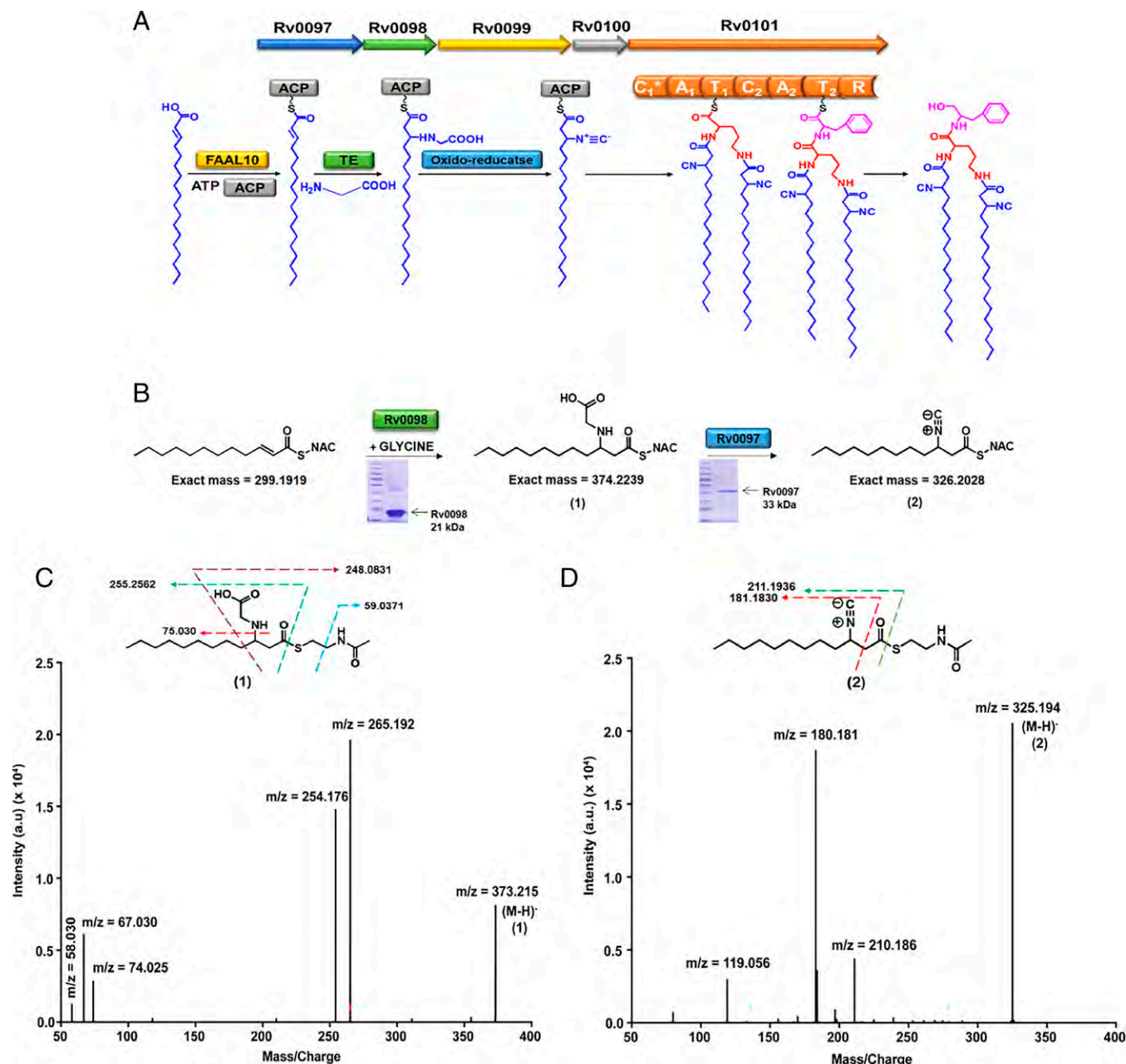
Mehdiratta et al.
Kupyaphores are zinc homeostatic metallophores required for colonization of *Mycobacterium tuberculosis*

PNAS | 5 of 12
https://doi.org/10.1073/pnas.2110293119

MICROBIOLOGY

Fig. 4. Biochemical analysis of *Mtb* Rv0097–Rv0101 gene cluster. (*A*) Schematic representation of putative biosynthetic steps for unknown metabolite production by *Mtb* Rv0097–Rv0101 gene cluster. *Mtb* harbors bimodular NRPS with seven catalytic domains. (*B*) Reaction scheme for enzymatic assays of purified Rv0098 and Rv0097 proteins with chemically synthesized C12-SNAC as substrate. (*C*) MS/MS spectra showing fragmentation products of glycine adduct of 2-dodecenoic-SNAC, 1, detected in the enzymatic assay with Rv0098 purified protein. No product could be detected in control reactions with no protein or no glycine. (*D*) MS/MS spectra of additional peak of *m/z* 326.2028 corresponding to isonitrile adduct of 2-dodecanoic-SNAC, 2, observed upon addition of Rv0097 purified protein to the Rv0098 assay conditions. The calculated masses for metabolites 1 and 2 are within 5-ppm mass error tolerance at MS1. All assays in *C* and *D* were performed in triplicates with reproducible results each time.

position. Previous studies had reported facile conversion of nitriles into amines on reaction with mild acid (41). Toward this end, protected β-amino fatty acid was coupled with L-ornithine and L-phenylalaninol sequentially, followed by deprotections resulting in the desired lipopeptide (*SI Appendix*, Fig. S7 *A–K*). Addition of formic acid to the biofilm metabolite extract resulted in disappearance of *m/z* for [M+H]⁺ ion 848.6987 (**VI**), having a retention time of 36 min, and a new peak could be observed at *m/z* for [M+H]⁺ ion 828. 73 with a retention time at 34 min. This new peak corresponded to the chemical synthetic standard compound (Fig.

5*E*). Additionally, both the parent peak and synthetic standard had identical MS/MS fragments (*SI Appendix*, Fig. S7*L*). Our studies thus identify and characterize a series of diacyl-diisonitrile lipopeptides from *Mtb* that consists of a dipeptide core of ornithine and phenylalaninol, where the amino-groups are acylated with isonitrile-containing fatty acyl chains ranging from C_{13} to C_{19}. Based on their metal acquisition functionality, we propose to name these *Mtb* diacyl-diisonitrile lipopeptides as "kupyaphores" (*Kupya* in Sanskrit refers to rare metals and *phores* means carrier in Latin), and this gene cluster could be recognized as *kupya A-E*.
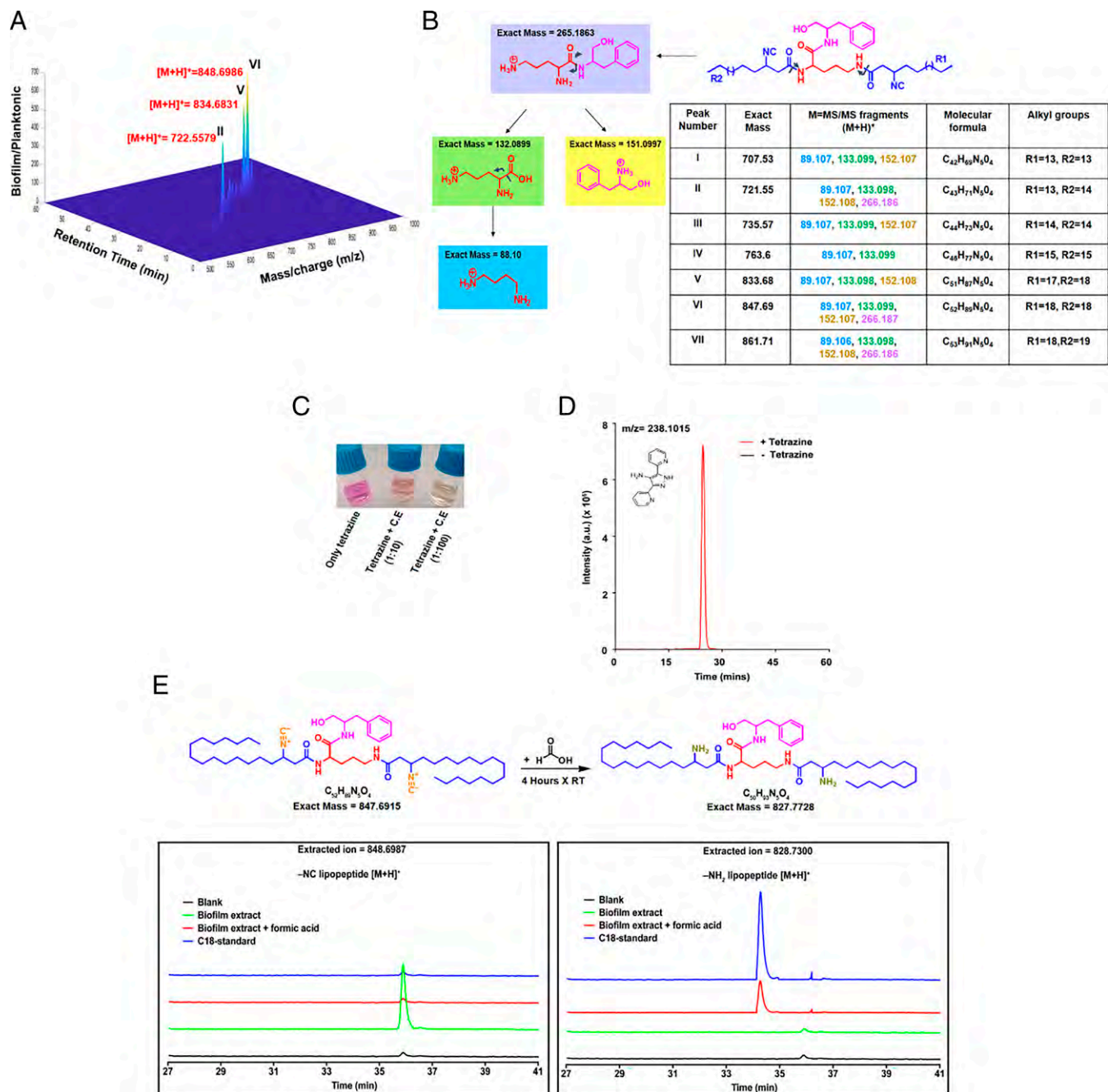
Fig. 5. Identification and characterization of kupyaphores from *Mtb* (*A*) Three-dimensional heat map plot shows masses uniquely identified from biofilm extracts of *Mtb* cultures but not planktonic cultures at various retention times. Three peaks with the highest fold-change between biofilm and planktonic cultures corresponded to m/z [M+H]$^+$ = 722.55 (II), 834.68 (V), and 848.69 (VI), are marked here in red. (*B*) MS/MS fragmentation pattern revealed common dipeptide backbone of ornithine and phenylalaninol in all the seven kupyaphore species (I–VII) observed in the complete spectra. Common fragments identified in the positive ion mode for all these masses show identical pattern. The predicted fragments are color coded along with their masses in the table. (*C*) Color change of Py-tetrazine from pink to yellow observed upon addition of WT *Mtb* biofilm extract. (*D*) Extracted ion chromatogram (EIC) for [M+H]$^+$ = 238.1014 corresponding to universal product, Py-aminepyrazole, in biofilm culture extract with and without tetrazine addition. (*E*) MS-based comparative analysis of EIC for biofilm organic extract and synthetic chemical standard at [M+H]$^+$ = 828.7300 and 848.6987. Addition of formic acid to biofilm organic extract shifts the mass of parent ion (m/z-848.6987) to that of synthetic chemical standard of amino substituted lipopeptide (m/z-828.73) concomitant with conversion of isonitrile to amine upon acid hydrolysis. The observed masses for I–VII are within 10 ppm mass error tolerance at MS1 or MS/MS for each mass.

Characterization of Kupyaphores in *Mtb*-Infected Mice Lungs and Human Clinical Strains. We next set out to understand the temporal regulation of this zinc acquisition machinery in the mouse infection model. Previous mice infection studies with this Δ*nrps* mutant in immunocompetent and immunocompromised mice showed reduced lung pathology with significantly increased mice survival rates (22). This phenotype was attributed to impairment

in the early infection events associated with the mutant *Mtb* strain. We therefore carefully dissected the early infection events from day 1 to day 28 (Fig. 6*A*). The mutant strain indeed showed more than one log-phase growth defect till week 3 postinfection, as compared to WT *Mtb* (Fig. 6*B*). This compromised growth of mutant *Mtb* highlights the significant role of this gene cluster in successful establishment of TB infection.

A portion of the lung tissue was also utilized for extraction of metabolites using ethyl acetate. LC-MS analysis of the tissue organic extracts of WT *Mtb*- and Δ*nrps*-infected lung tissues showed clear signals at *m/z* of $[M+H]^+ = 787.6315$, which corresponds to the *Mtb*-specific respiratory quinone, menaquinone (Fig. 6*C*). This confirms the presence of *Mtb* in the host lung tissue. Menaquinone peak was absent in the uninfected animal's lung tissue extract. Furthermore, we performed semiquantitative measurements for kupyaphore masses using multiple reaction monitoring (MRM) LC-MS analysis. Signals for kupyaphores **VI**, **II**, and **VII** species could be detected only from the WT *Mtb*-infected lung tissues and these were absent in Δ*nrps* mutant and uninfected lung tissue samples. Kupyaphore was absent on day 1 in WT *Mtb* and metabolite peaks built up from day 6 to day 15, then declined rapidly by day 21. Kupyaphores completely disappeared by day 28. Two series of kupyaphores could be identified based on their masses: one symmetrical corresponding to two C18 acyl chains of this lipopeptide and one asymmetrical, both modified with isonitrile groups (Fig. 6*D* and *SI Appendix*, Fig. S8 *A* and *B*). These studies suggest that kupyaphores are indeed an early response of *Mtb* to the host challenge and these metabolites disappear as the host–pathogen establish a more mutually coexistential harmony.

Furthermore, to recognize relevance of kupyaphores in pathophysiological context, we analyzed clinical strains obtained from TB patients for the production of these metallophores. MS analysis of ethyl acetate extract from four clinical *Mtb* strains showed robust expression of several of these kupyaphores (*SI Appendix*, Fig. S8*C*). These studies thus determine the significance of kupyaphores in *Mtb* pathogenesis.

Kupyaphores Are Secreted by *Mtb* for Zinc Acquisition. In order to capture zinc from the extracellular environment, kupyaphores would have to be secreted out of the *Mtb* cells. After chelating zinc, these zinc–kupyaphore complexes will have to be translocated across the *Mtb* cell envelope. To study kupyaphore trafficking, we compared the levels of kupyaphores in the *Mtb* cells grown in Sauton's medium and in the supernatant of cultures. While we observed low levels of kupyaphore species **I** to **VII** in the cells, significant enrichment was observed in the media supernatant under both low- and high-zinc conditions (Fig. 7*A*). As expected, no kupyaphores could be identified from the Δ*nrps*

grown in Sauton's media. Since Δ*nrps* cells do not grow in the minimal medium, we then asked whether exogenous addition of kupyaphores, produced by WT *Mtb*, could rescue the Δ*nrps* growth defect. Toward this end, we cultured the WT *Mtb* cells in Sauton's medium for 7 d. The conditioned supernatant from this WT *Mtb* cells was collected and added to the Δ*nrps* strain. We then followed the growth kinetics of the Δ*nrps* strain for 6 d and indeed observed robust growth for the Δ*nrps* culture supplemented with WT *Mtb* supernatant (Fig. 7*B*). As control, we had to use fresh medium, since the Δ*nrps* strain does not grow any further than the initial OD in the Sauton's medium. As expected, no growth was observed for Δ*nrps* cells supplemented by fresh medium (Fig. 7*B*). Clearly, the presence of kupyaphores in WT *Mtb* supernatant is able to rescue the growth defect by transporting essential micronutrient zinc.

Moreover, to assess whether secreted kupyaphores are involved in zinc uptake from the environment, we incubated WT, Δ*nrps*, and Δ*nrps:nrps Mtb* strains with 0.5 μM radioactive zinc-65 for 4 h. After 4 h, the internalized zinc-65 levels were measured in the cells. Significantly low radioactive counts were noted in Δ*nrps Mtb* cells, when compared to WT and Δ*nrps:nrps Mtb* strains, as measured by autoradiogram (Fig. 7 *C* and *D*). Together, these two studies directly demonstrate that absence of kupyaphores results in decreased zinc uptake efficiency, resulting in Δ*nrps* mutant growth defect. We also attempted to characterize dimeric zinc-bound kupyaphores using MS. Supernatant of WT *Mtb* grown with zinc supplementation showed doubly charged peaks that correspond to the kupyaphore–zinc complex and were absent in WT *Mtb* cultures grown in the absence of zinc in chelated Sauton's media (Fig. 7*E*). Our study thus demonstrates role of kupyaphore in restoration of bacterial zinc metabolic imbalance.

Putative Mechanism of Zinc Release from Kupyaphore by *Mtb* Isonitrile Hydratase. Since zinc is a redox-inert metal, the release of zinc from metallophores cannot follow the classic reductive release mechanism known for iron-siderophore. In the case of enterobactin, siderophore hydrolase is known to modify the scaffold mediating iron release (15). We therefore analyzed the *Mtb* genome to investigate the presence of putative isonitrile modifying enzyme. This enzyme activity (InhA) was first reported from *Pseudomonas putida* and was recently characterized (SfaF) from
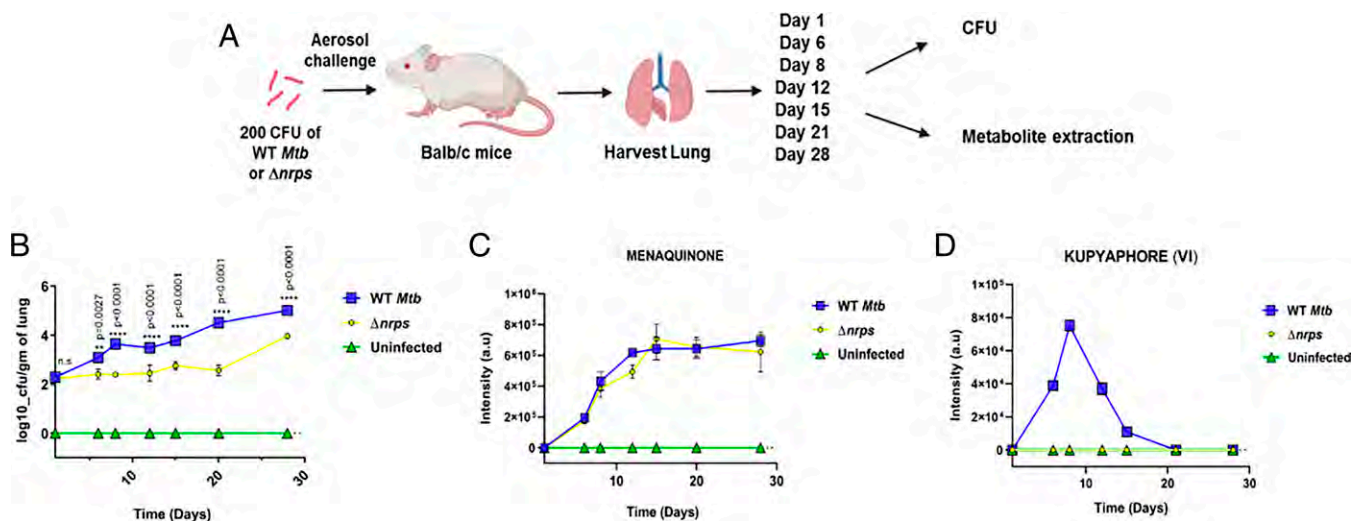

Fig. 6. Kupyaphores are required for establishment of *Mtb* infection in vivo. (*A*) Study design for murine TB infection by WT and Δ*nrps Mtb* strains. (*B*) Bacterial burden in the lungs of uninfected, WT and Δ*nrps Mtb* strains infected mice as measured by CFU enumeration. (*C*) MRM-based LC-MS measurements of *Mtb* respiratory quinone, menaquinone, from the lungs of uninfected, WT, and Δ*nrps Mtb*-infected mice. (*D*) Plot shows MRM-based semiquantitative LC-MS measurements of kupyaphore species: VI of *m/z* for $[M+H]^+ = 848.69$ from lungs of uninfected, WT, and Δ*nrps Mtb*-infected mice. Data represent mean ± SEM (*n* = 3 biological replicates per strain at each time point).

the SF2768 biosynthetic cluster of *S. thioluteus* (42, 43). Protein sequence analysis of the *Mtb* H37Rv genome coding sequence with InhA identified Rv0052 with an E-value score of $5e^{-31}$. Careful analysis of Rv0052 sequence with the three-dimensional structure (PDB ID code 3NON) indicated the absence of an important catalytic site (D17) from the annotated Rv0052. The gene Rv0052 is located between 57410 and 57973 bp in the genome of H37Rv. Analysis of upstream sequences revealed another start site 57 bp upstream in-frame with annotated Rv0052. A protein coding sequence of this open reading frame shows conservation of the catalytic residue D17. This protein was conserved across all *MTBC* strains and was absent from nonpathogenic mycobacterial species, where the *kupya* cluster is absent (*SI Appendix*, Fig. S9A).

To examine biochemical function, we cloned and expressed Rv0052 in BL21-DE3. The protein was purified and enzymatic assays were performed along with Rv0098 and Rv0097 (Fig. 8*A*). A clear peak corresponding to *m/z* of 243.176 for the *N*-formamide product could be observed only in the reactions supplemented with Rv0052 (*SI Appendix*, Fig. S9B). MS/MS fragmentation in the negative ion mode also provided further confidence to the hydration of isonitrile unit (Fig. 8*B*). Interestingly, Rv0052 expression was found to be significantly up-regulated by qRT-PCR only in low-zinc conditions and showed no induction under high-zinc conditions (Fig. 8*C*). Next, to investigate whether Rv0052 can directly modify kupyaphores, we incubated WT *Mtb* culture extract with purified Rv0052. Significant reduction in kupyaphore **VI** mass signals could be observed upon treatment with Rv0052, with concomitant appearance of new peaks corresponding to mono- and di-formamide kupyaphore analogs of *m/z* for [M+H]$^+$ = 866. 7021 and 884.7216, respectively (Fig. 8 *D* and *E*). Mass peaks corresponding to formamide and diformamide kupyaphore analogs could not be detected in the absence of Rv0052 (*SI Appendix*, Fig. S9C). These studies clearly demonstrate that Rv0052 can modify the isonitrile moiety of kupyaphore, which reduces the Lewis base character and destabilizes the coordinate complex bond with zinc. We thus propose that this could be a putative mechanism of zinc release from kupyaphores under low-zinc conditions.

Discussion

Given that there is virtually no free-zinc in the cell and that this micronutrient cannot be produced de novo, it becomes mandatory for pathogens to acquire these from the host pools. Bacteria have therefore evolved rather intricate molecular mechanisms of metal ion sensing, uptake, efflux, and allocation to maintain homeostasis (44). We herein decipher a mechanism of zinc acquisition whereby *Mtb* secretes zinc-selective metallophores, named kupyaphores, to support its intracellular survival. Kupyaphores belong to the recently identified family of diacyl-diisonitrile lipopeptides and is probably unique as a metabolite characterized directly from the host. We show that kupyaphores are produced by *Mtb* during biofilm formation or when grown at low- or high-zinc conditions in minimal medium and also from the lungs of *Mtb*-infected mice, as well as from clinical strains during early passages. Interestingly, transcriptional induction of the operon is more dramatic in macrophages than low- or high-zinc. The biosynthetic five-gene cluster consisting of bimodular NRPS is conserved only in pathogenic *MTBC* species. It is kind of surprising that this pathway is absent in saprophytic mycobacteria, which otherwise contain two types of siderophores for iron acquisition.

The chemical features of kupyaphores are typical of *Mtb* lipidic metabolites. Long-fatty acyl chains facilitate these molecules to transverse the complex *Mtb* cell envelope. The electron-rich isonitrile functionality forms a coordinate bond and the affinity for chelation to zinc metal ions is probably governed by

the structural architecture. In varying zinc conditions, kupyaphores shuttle in and out of the *Mtb* cells by using transporters that are yet to be characterized. Our studies show that the kupyaphore–zinc complex can be translocated inside. The intracellular release of zinc ions may be mediated by *Mtb*-encoded isonitrile hydratase (Rv0052) that modifies isonitriles to corresponding formamides. Surprisingly, we observed a stringent regulation of kupyaphores in both macrophages and in the lungs of infected mice, and these metabolites are present transiently during the early phase of infection. It will be interesting to identify mechanisms by which these metabolites are degraded. Recent study suggests that zinc-limited *Mtb* exhibit a global adaptive response that affects physiology, confers resiliency to oxidative stress, and possibly leads to increased virulence (45).

Kupyaphores show biological selectivity for the zinc and *kupya* biosynthetic cluster is transcriptionally activated under both low- and high-zinc levels. We therefore propose that kupyaphores may be potentially playing a role in both zinc acquisition, as well as quenching of toxic zinc levels (*SI Appendix*, Fig. S9D). Previous studies have indicated other isonitrile lipopeptides to chelate copper ions (20, 21, 46). Although at this stage we do not completely rule out the ability of kupyaphore to also bind to copper, the detailed binding affinities studies for various metal ions awaits total synthesis of kupyaphores. It is rather peculiar that the identification of these zinc chelating metallophores took this long, as the iron siderophores, mycobactins, of *Mtb* were discovered 70 y ago (47). The secretion of kupyaphores by WT *Mtb* actively augments free-zinc pools within phagosomes, as detected by zinc-selective dye. In contrast, the Δ*nrps* mutant shows significantly reduced signals and the levels of free-zinc are similar to uninfected macrophages. However, the total zinc pools within the macrophages in the case of mutant infection are maintained, suggesting that the Δ*nrps* mutant is unable to mobilize host zinc in the absence of kupyaphores. Our results thus suggest that kupyaphores can efficiently modulate host free-zinc redistribution and homeostasis; mechanisms underlying this triggered free-zinc redistribution require further investigation.

From a clinical perspective, low zinc levels have been reported in sera of TB patients as compared to healthy controls (48). Surprisingly, zinc supplementation does not restore zinc levels nor improve the clinical outcome in TB patients (49). Interestingly, studies with a mouse cachexia model of cancer have shown that proinflammatory responses modulate expression of zinc transporter, leading to a drop in serum zinc levels with concordant accumulation of zinc in tissues resulting in cachexia (50). With the discovery of kupyaphores as *Mtb* zinc acquisition machinery, it will be interesting to explore the dynamic processes of zinc mobilization and redistribution that could influence TB pathogenesis, and investigate relatively unexplored areas of TB-associated cachexia.

Methods

Bacterial Culture. *M. tuberculosis* H37Rv were routinely grown in Middlebrook 7H9 culture medium supplemented with 10% oleic acid-albumin-dextrose-catalase (OADC), 0.05% Tween-80 under shaking conditions or on Middlebrook 7H11 agar with 10% OADC at 37 °C. For metal studies, *Mtb* strains were grown in chelated Sauton's medium, details of which are provided in the *SI Appendix*. *Mtb* biofilms were grown in Sauton's medium (without Tween-80 or tyloxapol) by incubation without shaking at 37 °C for 5 wk under humidified conditions.

Determination of Total Metal Ions in In Vitro Bacterial Cultures. Briefly, 0.8 to 1.0 OD WT *Mtb* cultures grown in chelated Sauton's medium supplemented with ZnSO$_4$ were lysed by boiling in 0.1% SDS and 0.2% HNO$_3$ for 15 min and total metal concentrations were measured by ICP-MS (ThermoXcaliber II). Details provided in the *SI Appendix*.

Determination of Free Zinc in Macrophage Infection Studies. Macrophage cultures uninfected or infected with mCherry labeled *Mtb* strains were stained with 0.5 μM FZ3-AM and fixed with 4% paraformaldehyde. Details of staining
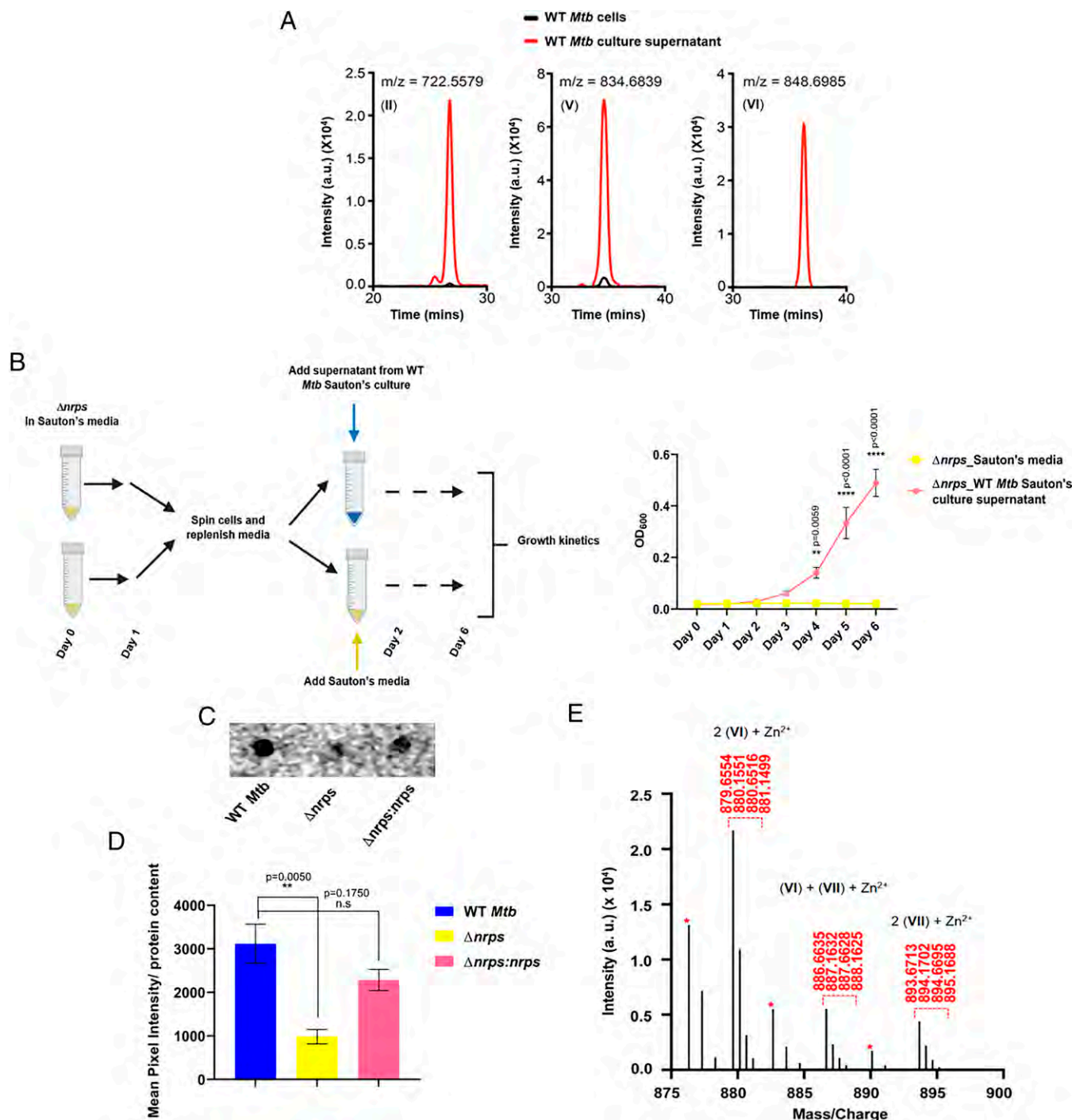
Mehdiratta et al.
Kupyaphores are zinc homeostatic metallophores required for colonization
of *Mycobacterium tuberculosis*

PNAS | 9 of 12
https://doi.org/10.1073/pnas.2110293119

Fig. 7. Kupyaphores are secreted by *Mtb* for zinc acquisition (*A*) EIC of kupyaphore species II, V, and VI corresponding to *m/z* for [M+H]$^+$ = 722.55, 834.68, and 848.69 detected from organic extracts of supernatant and cells of WT *Mtb* grown in Sauton's medium. (*B*) Study design and growth kinetics of Δ*nrps* supplemented with supernatant from WT *Mtb* cultures as compared to Δ*nrps* grown in Sauton's medium alone. Addition of WT *Mtb* supernatant rescued the growth defect observed in Δ*nrps*. (*C*) Radioactive zinc-65 feeding of WT, Δ*nrps*, and Δ*nrps:nrps Mtb* strains. After 4 h, cells were lysed and spotted for estimating intracellular zinc-65 accumulation by autoradiography. (*D*) Quantitation of autoradiograph signals of three strains as mean pixel intensity in arbitrary units normalized to protein content estimated for each strain. (*E*) MS1 spectra showing doubly charged peaks corresponding to dimeric kupyaphore-zinc metabolites from WT *Mtb* extract supplemented with zinc. Putative zinc adducts for both homodimeric and heterodimeric kupyaphore species could be detected. Single charged ions are marked with red asterisks. The corresponding mass peaks were absent from WT *Mtb* supernatant extract, which was not supplemented with zinc. The calculated masses for metabolites are within 5 ppm mass error tolerance at MS1. Data represents mean ± SEM (*n* = 3 biological replicates).

protocol are provided in the *SI Appendix*. Fixed cells were then mounted with DAPI. DAPI$^+$, mCherry$^+$, and FZ3 green$^+$ cells were selected for each of the triplicate samples by confocal microscopy using Zeiss LSM980 and mean pixel intensity for FZ3 signals was analyzed using ImageJ.

Extraction and Analysis of Kupyaphores from *Mtb* Cultures. Middlebrook 7H9 grown planktonic and biofilm cultures of WT *Mtb*, Δ*nrps*, and Δ*nrps:nrps* were harvested and weighed. Supernatant and cells of the WT *Mtb* strain from planktonic cultures of chelated Sauton's medium
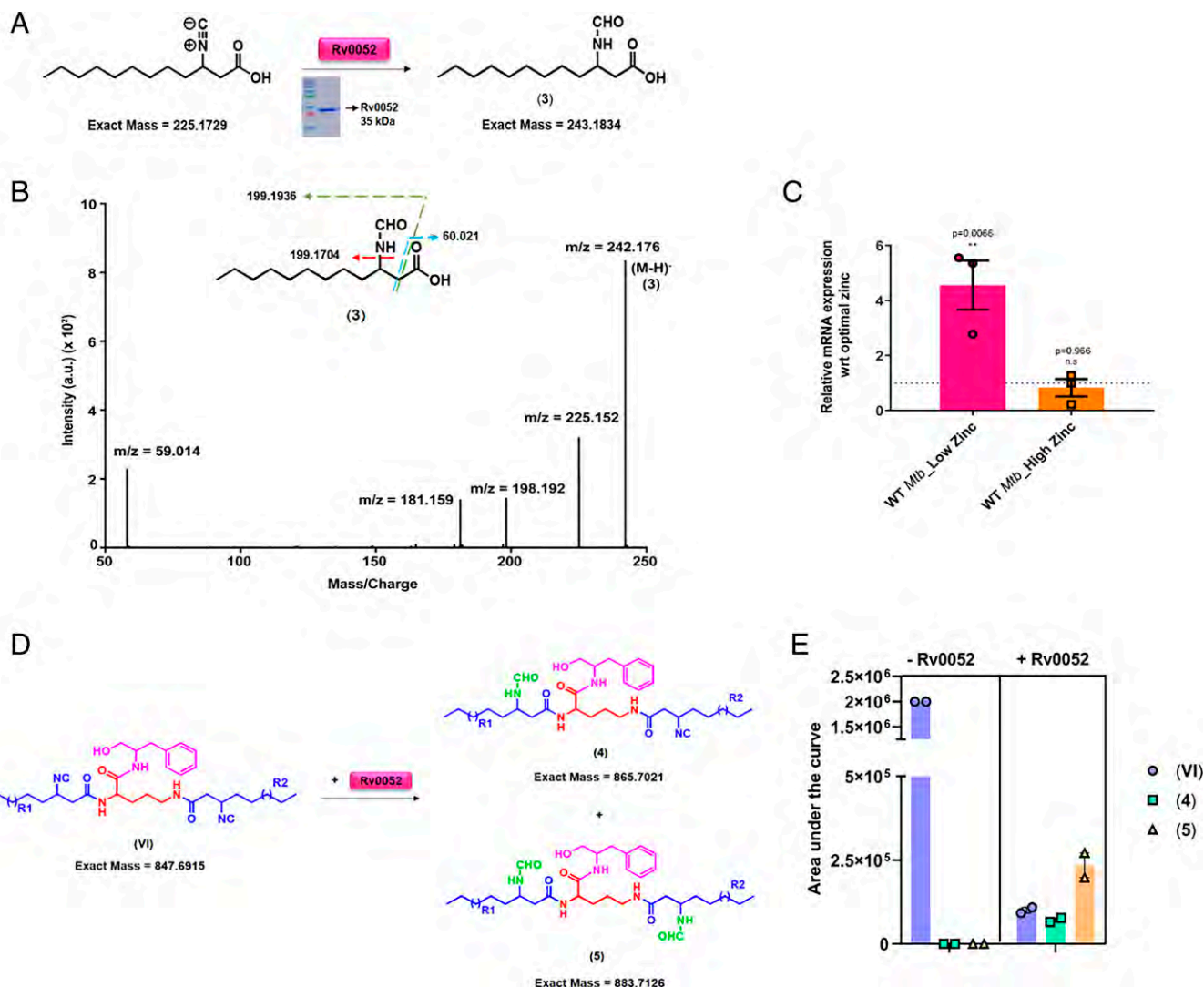
Mehdiratta et al.
Kupyaphores are zinc homeostatic metallophores required for colonization
of *Mycobacterium tuberculosis*

Fig. 8. Release of zinc from kupyaphores is mediated by *Mtb* isonitrile hydratase. (*A*) Reaction scheme for in vitro enzymatic assay of Rv0052. (*B*) MS/MS spectra with fragmentation pattern and products marked for expected product 3, confirming the presence of formamide product in the assay. The observed masses are within 10 ppm mass error tolerance at MS1 or MS/MS for each mass. (*C*) qRT based mRNA expression analysis of Rv0052 in WT *Mtb* under low- and high-zinc condition as compared to optimal-zinc growth condition. (*D*) Reaction scheme for Rv0052 enzymatic assay with kupyaphores. (*E*) Relative MS intensities of kupyaphore species VI of *m/z* for [M+H]$^+$= 848.69, and corresponding monoformamide 4 and diformamide 5 analogs in WT *Mtb* extract treated with or without Rv0052. The calculated masses for metabolites are within 5 ppm mass error tolerance at MS1. All assays in *B* and *E* were performed in triplicates and duplicates, respectively, with reproducible results each time.

supplemented with and without zinc were also collected separately. Low-molecular-weight molecules were then extracted by ethyl acetate and analyzed by an information dependent acquisition scanning on a Sciex X500R QTOF mass spectrometer fitted with an ExionLC UPHLC system using the SciexOS software using previously reported methods (36, 37). Details are provided in the *SI Appendix*.

Mtb Metabolite Isolation upon Murine TB Infection. For *Mtb* metabolite extraction from mice, 0.1 g of lung tissue was taken from left apical lobe of uninfected and infected mice at indicated time points. Low-molecular-weight metabolites were extracted by homogenizing tissues in ethyl acetate (36, 37). All the species analyzed were quantified using the MRM-HR LC-MS method on a Sciex X500R QTOF mass spectrometer, details of which are provided in the *SI Appendix*.

Radioactive Zinc-65 Uptake Assay. An equal number of WT, Δ*nrps*, and Δ*nrps:nrps Mtb* cells were incubated with 0.5 μM of radioactive zinc-65 for 4 h. After 4 h, cells were lysed. Intracellular radioactive count was then measured by autoradiography and quantitated using ImageJ analysis. Mean pixel intensity so obtained was then normalized to protein content estimated by BCA for each sample. Details are provided in the *SI Appendix*.

Statistical Analysis. GraphPad Prism 8 software was used for statistical analysis. Statistical significance was analyzed by Student's *t* test or one-way or two-way ANOVA, with *P* values mentioned for each data point when applicable. Data were plotted as the mean, with error bars representing SEM of three biological replicates for all experiments, unless stated otherwise.

Ethics Declaration. All mouse studies described in this paper received formal approval from the National Institute of Immunology–Institutional Animal Ethics Committee (NII-IAEC 440/17) following the guidelines outlined by the Committee for the Purpose of Control and Supervision of Experiments on Animals, Government of India. Studies on clinical strains isolated from TB patients described in this paper have approval from Institutional Review Board (IRB) Christian Medical College, Vellore (IRB Min No.7239). The IRB reviewed and discussed the project after going through IRB application format, patient information sheet, consent form, and other documents. Informed consent was taken from all the participants involved in the study. All of these documents were submitted to Institutional Human Ethical Committee of the Council of Scientific and Industrial Research–Institute of Genomics and Integrative Biology.

Data Availability. Detailed codes used for the analysis have been submitted to the GitHub repository (https://github.com/viv3kanand/MTU-Manuscript/). The datasets generated during or analyzed during the current study can be

Mehdiratta et al.
Kupyaphores are zinc homeostatic metallophores required for colonization
of *Mycobacterium tuberculosis*

PNAS | 11 of 12
https://doi.org/10.1073/pnas.2110293119

1. E. J. Rubin, Troubles with tuberculosis prevention. *N. Engl. J. Med.* **370**, 375–376 (2014).
2. S. H. Kaufmann, S. T. Cole, V. Mizrahi, E. Rubin, C. Nathan, *Mycobacterium tuberculosis* and the host response. *J. Exp. Med.* **201**, 1693–1697 (2005).
3. O. Neyrolles, F. Wolschendorf, A. Mitra, M. Niederweis, Mycobacteria, metals, and the macrophage. *Immunol. Rev.* **264**, 249–263 (2015).
4. N. A. Zondervan, J. C. J. van Dam, P. J. Schaap, V. A. P. Martins Dos Santos, M. Suarez-Diez, Regulation of three virulence strategies of *Mycobacterium tuberculosis*: A success story. *Int. J. Mol. Sci.* **19**, 347 (2018).
5. M. I. Hood, E. P. Skaar, Nutritional immunity: Transition metals at the pathogen-host interface. *Nat. Rev. Microbiol.* **10**, 525–537 (2012).
6. D. Wagner *et al.*, Elemental analysis of *Mycobacterium avium*-, *Mycobacterium tuberculosis*-, and *Mycobacterium smegmatis*-containing phagosomes indicates pathogen-induced microenvironments within the host cell's endosomal system. *J. Immunol.* **174**, 1491–1500 (2005).
7. H. Botella *et al.*, Mycobacterial p(1)-type ATPases mediate resistance to zinc poisoning in human macrophages. *Cell Host Microbe* **10**, 248–259 (2011).
8. F. Wolschendorf *et al.*, Copper resistance is essential for virulence of *Mycobacterium tuberculosis*. *Proc. Natl. Acad. Sci. U.S.A.* **108**, 1621–1626 (2011).
9. A. Maciag *et al.*, Global analysis of the *Mycobacterium tuberculosis* Zur (FurB) regulon. *J. Bacteriol.* **189**, 730–740 (2007).
10. A. Mikhaylina, A. Z. Ksibe, D. J. Scanlan, C. A. Blindauer, Bacterial zinc uptake regulator proteins and their regulons. *Biochem. Soc. Trans.* **46**, 983–1001 (2018).
11. Y. Li *et al.*, Zinc depletion induces ribosome hibernation in mycobacteria. *Proc. Natl. Acad. Sci. U.S.A.* **115**, 8191–8196 (2018).
12. G. M. Rodriguez, M. I. Voskuil, B. Gold, G. K. Schoolnik, I. Smith, ideR, An essential gene in mycobacterium tuberculosis: Role of IdeR in iron-dependent gene expression, iron metabolism, and oxidative stress response. *Infect. Immun.* **70**, 3371–3381 (2002).
13. A. Chao, P. J. Sieminski, C. P. Owens, C. W. Goulding, Iron acquisition in *Mycobacterium tuberculosis*. *Chem. Rev.* **119**, 1193–1220 (2019).
14. R. Krithika *et al.*, A genetic locus required for iron acquisition in *Mycobacterium tuberculosis*. *Proc. Natl. Acad. Sci. U.S.A.* **103**, 2069–2074 (2006).
15. N. A. Larsen, H. Lin, R. Wei, M. A. Fischbach, C. T. Walsh, Structural characterization of enterobactin hydrolase IroE. *Biochemistry* **45**, 10184–10190 (2006).
16. G. Ghssein *et al.*, Biosynthesis of a broad-spectrum nicotianamine-like metallophore in *Staphylococcus aureus*. *Science* **352**, 1105–1109 (2016).
17. S. Lhospice *et al.*, *Pseudomonas aeruginosa* zinc uptake in chelating environment is primarily mediated by the metallophore pseudopaline. *Sci. Rep.* **7**, 17132 (2017).
18. K. P. Grim *et al.*, The metallophore staphylopine enables *Staphylococcus aureus* to compete with the host for zinc and overcome nutritional immunity. *MBio* **8**, e01281-e17 (2017).
19. J. R. Morey, T. E. Kehl-Fie, Bioinformatic mapping of opine-like zincophore biosynthesis in bacteria. *mSystems* **5**, e00554-e20 (2020).
20. L. Wang *et al.*, Diisonitrile natural product SF2768 functions as a chalkophore that mediates copper acquisition in *Streptomyces thioluteus*. *ACS Chem. Biol.* **12**, 3067–3075 (2017).
21. N. C. Harris *et al.*, Biosynthesis of isonitrile lipopeptides by conserved nonribosomal peptide synthetase gene clusters in Actinobacteria. *Proc. Natl. Acad. Sci. U.S.A.* **114**, 7025–7030 (2017).
22. K. Bhatt *et al.*, A nonribosomal peptide synthase gene driving virulence in *Mycobacterium tuberculosis*. *MSphere* **3**, e00352-e18 (2018).
23. O. A. Trivedi *et al.*, Dissecting the mechanism and assembly of a complex virulence mycobacterial lipid. *Mol. Cell* **17**, 631–643 (2005).
24. B. Baral, A. Akhgari, M. Metsä-Ketelä, Activation of microbial secondary metabolic pathways: Avenues and challenges. *Synth. Syst. Biotechnol.* **3**, 163–178 (2018).
25. D. R. Campbell *et al.*, Mycobacterial cells have dual nickel-cobalt sensors: Sequence relationships and metal sites of metal-responsive repressors are not congruent. *J. Biol. Chem.* **282**, 32298–32310 (2007).
26. R. A. Festa *et al.*, A novel copper-responsive regulon in *Mycobacterium tuberculosis*. *Mol. Microbiol.* **79**, 133–148 (2011).
27. E. Tinaztepe *et al.*, Role of metal-dependent regulation of ESX-3 secretion in intracellular survival of *Mycobacterium tuberculosis*. *Infect. Immun.* **84**, 2255–2263 (2016).
28. D. Giovannini *et al.*, A new *Mycobacterium tuberculosis* smooth colony reduces growth inside human macrophages and represses PDIM Operon gene expression. Does an heterogeneous population exist in intracellular mycobacteria? *Microb. Pathog.* **53**, 135–146 (2012).
29. J. P. Richards, W. Cai, N. A. Zill, W. Zhang, A. K. Ojha, Adaptation of *Mycobacterium tuberculosis* to biofilm growth is genetically linked to drug tolerance. *Antimicrob. Agents Chemother.* **63**, 1213–1219 (2019).
30. P. Arora *et al.*, Mechanistic and functional insights into fatty acid activation in *Mycobacterium tuberculosis*. *Nat. Chem. Biol.* **5**, 166–173 (2009).
31. H. C. Wong, G. Liu, Y. M. Zhang, C. O. Rock, J. Zheng, The solution structure of acyl carrier protein from *Mycobacterium tuberculosis*. *J. Biol. Chem.* **277**, 15874–15880 (2002).
32. N. C. Harris *et al.*, Isonitrile formation by a non-heme iron(II)-dependent oxidase/decarboxylase. *Angew. Chem. Int. Ed. Engl.* **57**, 9707–9710 (2018).
33. C. T. Walsh, Insights into the chemical logic and enzymatic machinery of *NRPS* assembly lines. *Nat. Prod. Rep.* **33**, 127–135 (2016).
34. S. Kapur, C. Khosla, Biochemistry: Fit for an enzyme. *Nature* **454**, 832–833 (2008).
35. A. Chhabra *et al.*, Nonprocessive [2 + 2]e- off-loading reductase domains from mycobacterial nonribosomal peptide synthetases. *Proc. Natl. Acad. Sci. U.S.A.* **109**, 5681–5686 (2012).
36. D. S. Kelkar *et al.*, A chemical-genetic screen identifies ABHD12 as an oxidized-phosphatidylserine lipase. *Nat. Chem. Biol.* **15**, 169–178 (2019).
37. N. Khandelwal *et al.*, Fatty acid chain length drives lysophosphatidylserine-dependent immunological outputs. *Cell Chem. Biol.* **28**, 1169–1179.e6 (2021).
38. M. Z. Ansari, G. Yadav, R. S. Gokhale, D. Mohanty, *NRPS*-PKS: A knowledge-based resource for analysis of *NRPS*/PKS megasynthases. *Nucleic Acids Res.* **32**, W405–W413 (2004).
39. B. O. Bachmann, J. Ravel, Chapter 8. Methods for in silico prediction of microbial polyketide and nonribosomal peptide biosynthetic pathways from DNA sequence data. *Methods Enzymol.* **458**, 181–217 (2009).
40. Y. B. Huang, W. Cai, A. Del Rio Flores, F. F. Twigg, W. Zhang, Facile discovery and quantification of isonitrile natural products via tetrazine-based click reactions. *Anal. Chem.* **92**, 599–602 (2020).
41. B. D. Ames *et al.*, Crystal structure and biochemical studies of the trans-acting polyketide enoyl reductase LovC from lovastatin biosynthesis. *Proc. Natl. Acad. Sci. U.S.A.* **109**, 11144–11149 (2012).
42. M. Goda *et al.*, Isonitrile hydratase from *Pseudomonas putida* N19-2. Cloning, sequencing, gene expression, and identification of its active acid residue. *J. Biol. Chem.* **277**, 45860–45865 (2002).
43. M. Zhu *et al.*, Tandem hydration of diisonitriles triggered by isonitrile hydratase in *Streptomyces thioluteus*. *Org. Lett.* **20**, 3562–3565 (2018).
44. K. Subramanian Vignesh, G. S. Deepe Jr., Immunological orchestration of zinc homeostasis: The battle between host mechanisms and pathogen defenses. *Arch. Biochem. Biophys.* **611**, 66–78 (2016).
45. A. Dow *et al.*, Zinc limitation triggers anticipatory adaptations in *Mycobacterium tuberculosis*. *PLoS Pathog.* **17**, e1009570 (2021).
46. Y. Xu, D. S. Tan, Total synthesis of the bacterial diisonitrile chalkophore SF2768. *Org. Lett.* **21**, 8731–8735 (2019).
47. G. A. Snow, Isolation and structure of mycobactin T, a growth factor from Mycobacterium tuberculosis. *Biochem. J.* **97**, 166–175 (1965).
48. H. Ghulam *et al.*, Status of zinc in pulmonary tuberculosis. *J. Infect. Dev. Ctries.* **3**, 365–368 (2009).
49. M. E. Visser *et al.*, The effect of vitamin A and zinc supplementation on treatment outcomes in pulmonary tuberculosis: A randomized controlled trial. *Am. J. Clin. Nutr.* **93**, 93–100 (2011).
50. G. Wang *et al.*, Metastatic cancers promote cachexia through ZIP14 upregulation in skeletal muscle. *Nat. Med.* **24**, 770–781 (2018).

12 of 12 | **PNAS**
https://doi.org/10.1073/pnas.2110293119

Mehdiratta et al.
Kupyaphores are zinc homeostatic metallophores required for colonization of *Mycobacterium tuberculosis*